

# Data Driven Modeling of Interfacial Traction Separation Relations using Thermodynamic Consistent Neural Network (TCNN)

Congjie Wei<sup>1</sup>, Jiaxin Zhang<sup>2\*</sup>, Kenneth M. Liechti<sup>3</sup>, Chenglin Wu<sup>1\*</sup>,

<sup>1</sup>Department of Civil, Architectural, and Environmental Engineering  
Missouri University of Science and Technology, Rolla, MO, USA

<sup>2</sup>Oak Ridge National Laboratory, Oak Ridge, TN 37830

<sup>3</sup>Cockrell School of Engineering

The University of Texas at Austin, Austin, TX, USA

\* Corresponding author E-mail: [zhangj@ornl.gov](mailto:zhangj@ornl.gov), [wuch@mst.edu](mailto:wuch@mst.edu)

## Abstract

For multilayer structures in thin substrate systems, the interfacial failure is one of the most important reliability issues. The traction-separation relations (TSR) along fracture interface, which is often a complicated mixed-mode problem, is usually adopted as a representative of the adhesive interactions of a biomaterial system. However, the existing theoretical models lack complexity and are not able to fit with real-world TSRs obtained with end loaded split beam (ELS) experiments. However, the neural network fits well with the experimental data along the loading paths but fails to obey physical laws for area not covered by the training data sets, due to the lack of mechanics in pure neural network fitting with training data sets. In this paper, a thermodynamic consistent neural network (TCNN) is established to model the interface TSRs with sparse training data sets. Three thermodynamic consistent conditions are considered and implemented with neural network model: thermodynamic consistent condition, local fastest energy dissipation direction condition and fixed ratio between normal and tangential tractions when loaded along fixed phase angle loading paths condition. By treating these thermodynamic consistent conditions as constraints and implementing as loss function terms, the whole traction surface is constrained to provide reasonable results. The feasibility of this approach is approved by comparing the modeling results with different number of physical constraints. Moreover, the Bayesian optimization algorithm is adopted to optimize the weighting factors of the TCNN to overcome the convergence issue when multiple constraints are in present. The numerical implementation results demonstrated well behaved prediction of mixed-mode traction separation surfaces in terms of high agreement with experimental data and damage mechanics contained thermodynamic consistencies. The proposed approach opens doors to a new autonomous, point-to-point constitutive modeling concept for interface mechanics.

**Keywords:** Interface mechanics; Physics constrained neural networks; Machine Learning; Bayesian optimization

## Nomenclature

<b>Abbreviation</b>	<b>Meaning</b>
TSR	Traction separation relation
ELS	End loaded split beam
CZM	Cohesive zone model
MSE	Mean squared error
TC	Thermodynamic consistent
TC1	Monotonic energy dissipation condition/constraint
TC2	Local fastest descending condition/constraint
TC3	Conservative loading path condition/constraint
DNN	Deep neural network
TCNN	Thermodynamic consistent neural network model
BO	Bayesian optimization

<b>Symbol</b>	<b>Description</b>
$\delta_n, \delta_t$	Normal and tangential separation
$\sigma_n, \sigma_t$	Normal and tangential traction
$ \delta ,  \sigma $	Separation norm, traction norm
$\phi$	Phase angle
$J_n, J_t$	Normal and tangential J-integral
$d_n, d_t$	Normal and tangential damage parameter
$\Gamma_n, \Gamma_t$	Normal and tangential toughness
$X, Y$	Input and output data sets
$MSE_0$	Loss function term corresponding to mean squared error
$MSE_1, MSE_2, MSE_3$	Loss function terms corresponding to TC1, TC2 and TC3 constraints
$\lambda_0$	Weighting factor corresponding to mean squared error
$\lambda_1, \lambda_2, \lambda_3$	Weighting factors corresponding to TC1, TC2 and TC3 constraints
$\epsilon_{phi}$	Angle difference
$Vi_0_1, Vi_0_2, Vi_0_3$	Violations to TC1, TC2 and TC3 conditions

$V_{iO_{1,norm}}, V_{iO_{2,norm}}, V_{iO_{3,norm}}$  Normalized violations to TC1, TC2 and TC3 conditions

## 1. Introduction

Firstly proposed by Dugdale and Barrenblatt [1, 2], cohesive zone models (CZM) have been most widely adopted to describe nonlinear fracture process, especially for the interfacial fracture where fracture paths are often pre-determined [3-6]. Typically, the CZM models take the pre-determined traction-separation relations (TSR) as input through either cohesive element or cohesive contact formulation in finite element method (FEM) to describe the interfacial fractures. Based on how traction-separation relations (TSR) are implemented, CZM models can be divided into displacement-based (or non-potential-based) models and potential-based models [7]. The non-potential based models typically requires specific pre-determined TSR including the bilinear softening [8], cubic-polynomial [9], linear-softening [10] and exponential [11, 12]. However, the physics behind the TSR are typically not considered in the non-potential based model.

To ensure the input TSR conform with the thermodynamics, the potential-based models are proposed where the TSR are defined based on the concept of cohesive energy potential where normal and tangential separations are adopted as independent variables. Cohesive tractions are defined as gradients of the cohesive energy potentials over separations for the softening stage. Needleman [13] pioneered the potential based approach by introducing cubic-linear and exponential interfacial debonding potentials. Freed and Bank-Sills [14] extended the application to the bi-material systems. Other types of potentials were also explored, including atomistic potential relating metallic binding energies to lattice parameters [15], exponential-periodic potential adopting large tangential displacement jump [16] and generalized exponential-periodic potential considering the relation between cleavage decohesion and dislocation nucleation [17]. These potential-based models can capture ideal physics relationship at the interfaces and have certain flexibility to accommodate some of the experimentally observed behaviors. However, when complex interfacial failure mechanisms are involved, e.g., friction and bearing that often observed, the potential-based model often faces challenges in fitting the experimental data. Therefore, it is a need to develop a data-driven approach to model interfacial TSR, which can capture the richness of the experimental data as well as be consistent with the thermodynamic consistent (TC) conditions. To this end, we seek a way to combine the data-drive approach,

specifically the deep learning approach, with the TC constraints to deliver a universal approach to model the interfacial TSR directly from the experimental data.

Deep learning approach especially the deep neural network (DNN) has already been incorporated into the computational fluid mechanics, where it is used to solve the governing partial differential equations (PDEs) of the fluid field [18-20] and constitutive modeling in plasticity [21-23]. In the solution, the DNN is utilized to generate possible solutions in terms of the displacement or velocity field that can satisfy the required PDEs. This approach has given the authors the inspiration to generate TSR that can satisfy the thermodynamics governing equations. Specifically, the authors propose to utilize the DNN to “learn” the TSR extracted from the experiment for certain mode-mix and then predict the TSR for the mode-mix at which the experimental data are not available. During the TSR generation, the TC constraints including the enforcement on the positive energy dissipation, the local maximum in energy dissipation, as well as the conservation of interfacial fracture toughness, have been embedded into the DNN model to form a thermodynamic consistent neural network (TCNN) for the TSR modeling. The hyperparameter system, which is used for tuning the learning process, plays an essential role on the performance of neural networks. When inappropriate hyperparameter sets are adopted, TCNN could result in much elongated time period to reach convergence, missing important patterns in TSRs and lack of robustness. Efforts have been made on algorithms for hyperparameter optimization, other than grid or random search, which is time consuming and computationally costly, optimization algorithms, Bayesian (BO) optimization [24, 25], tree structured Parzen estimators [26, 27] for example, have been proposed to accelerate this process. We then employed the TCNN to model the TSR as a surface in the three-dimensional space formed by either normal or shear traction, and corresponding normal and shear separations. Not only our modeled results using the TCNN show close agreement with our experimental measured line data, but also conform the required TC conditions very well.

The remainder of this paper is organized as follows. Theories related to our work are presented in Section 2 including the introduction of TSRs, TC conditions. Section 3 includes the constructions of TCNN that consists of the neural network & TC conditions, as well as the weighting factors optimization with Bayesian optimization algorithms. Section 4 presents the TSR modeling results with analytical CZM models, regular neural networks and TCNN. Section 5 closes this paper with discussion and conclusions. Detailed derivations, supplementary figures and tables are included in Supplementary Information.

## 2. Interfacial TSR and TC conditions

### 2.1 Interfacial traction separation relations (TSR)

For a two-layer structure undergoing interfacial fracture process as shown in Fig. 1a, a cohesive layer in between these two evolved substrates provides tractions. This cohesive layer is assumed to be homogeneous, which enables us to consider it as an assembly of identical “springs” connecting the two layers. The interfacial fracture process is then reproduced with the elongation and failure process of each “spring” along the interface. As shown in Fig. 1a-b, for a stretched spring connecting the upper and lower layer, the normal and tangential tractions ( $\sigma_n, \sigma_t$ ) change correspondingly with the normal and tangential separations ( $\delta_n, \delta_t$ ), which are defined by the change of the relative distances between the end points of the “spring”. Depending on the loading and boundary conditions, the ratio between the tangential and normal separations (i.e., the mode-mix) varies. To quantitatively describe this relation, the vectorial separation is defined as the Euclidean norm of normal and tangential separation components, shown as  $|\delta|$  in Eq. 1a. The mode mix is represented by the phase angle, which is defined as the arctangent of the ratio between normal and tangential separations, shown as  $\phi$  in Eq. 1b. Similarly, the vectorial traction is defined as  $|\sigma|$  in Eq. 1c.

$$|\delta| = \sqrt{\delta_n^2 + \delta_t^2} \quad (1a)$$

$$\phi = \text{atan}\left(\frac{\delta_t}{\delta_n}\right) \quad (1b)$$

$$|\sigma| = \sqrt{\sigma_n^2 + \sigma_t^2} \quad (1c)$$

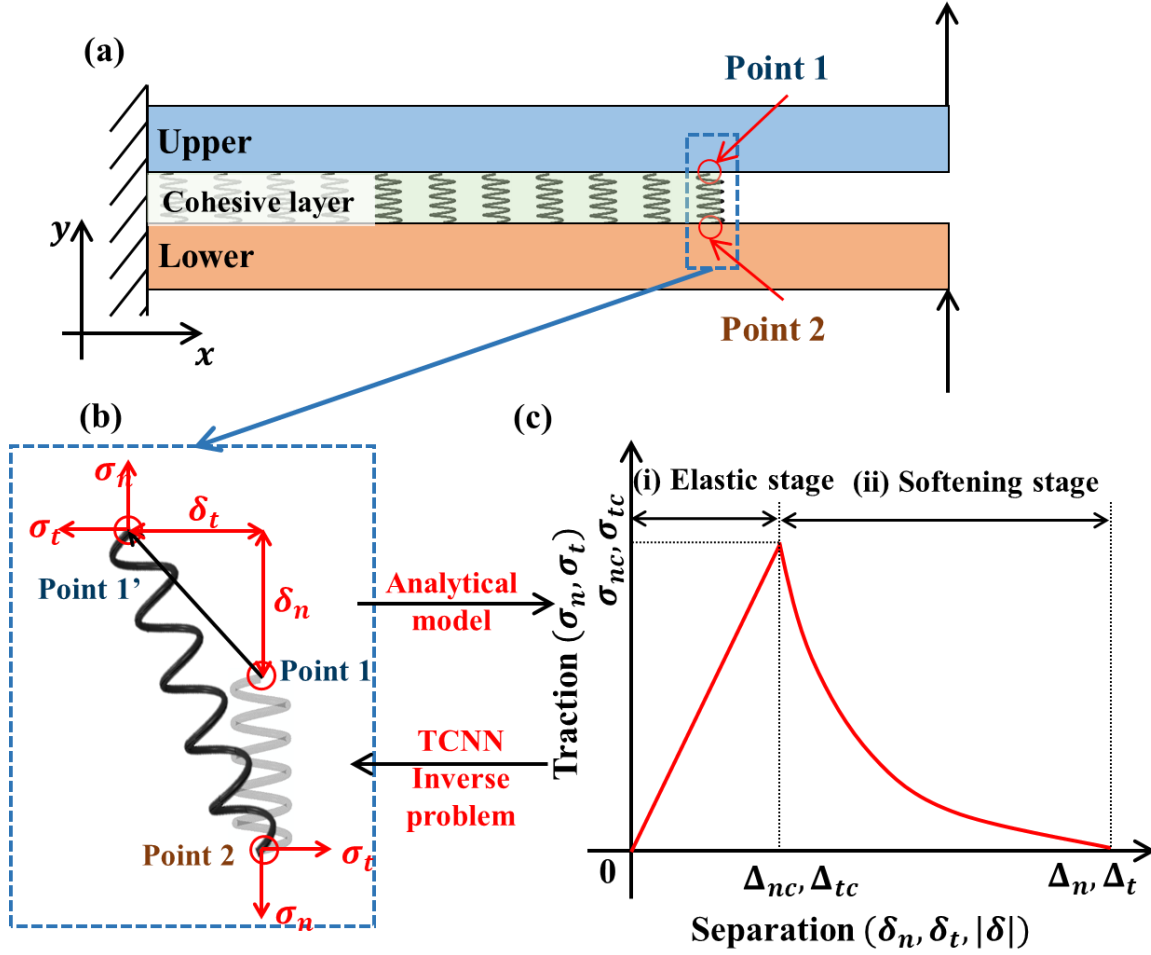


Fig. 1. (a) Schematics of a beam under end loaded split experiment. (b) Traction and separations for one spring. (c) A typical traction separation relation indicating two-stage response.

The traction-separation relation (TSR), i.e.,  $\sigma_n(\delta_n, \delta_t)$ ,  $\sigma_t(\delta_n, \delta_t)$ , constitutes the interfacial mechanical property. Typically, a TSR has two stages: (i) the elastic stage during which the traction increases along with separations, and (ii) the softening stage where the traction decreases with increasing separation. Fig. 1c shows a typical TSR where the elastic stage has a linear profile and the softening stage follows an exponential one. To examine the features of the TSR data in detail, we plot the mixed-mode TSR extracted for silicon-epoxy interface [28] in Fig. 2a-b. Notice that the TSR data for both normal and tangential directions are not smooth. Sharp peaks or discontinuity in gradients are commonly observed as shown in Fig. 2c-d. These features make it almost impossible to be modeled by the smooth functions, which are typically used in the existing approaches.

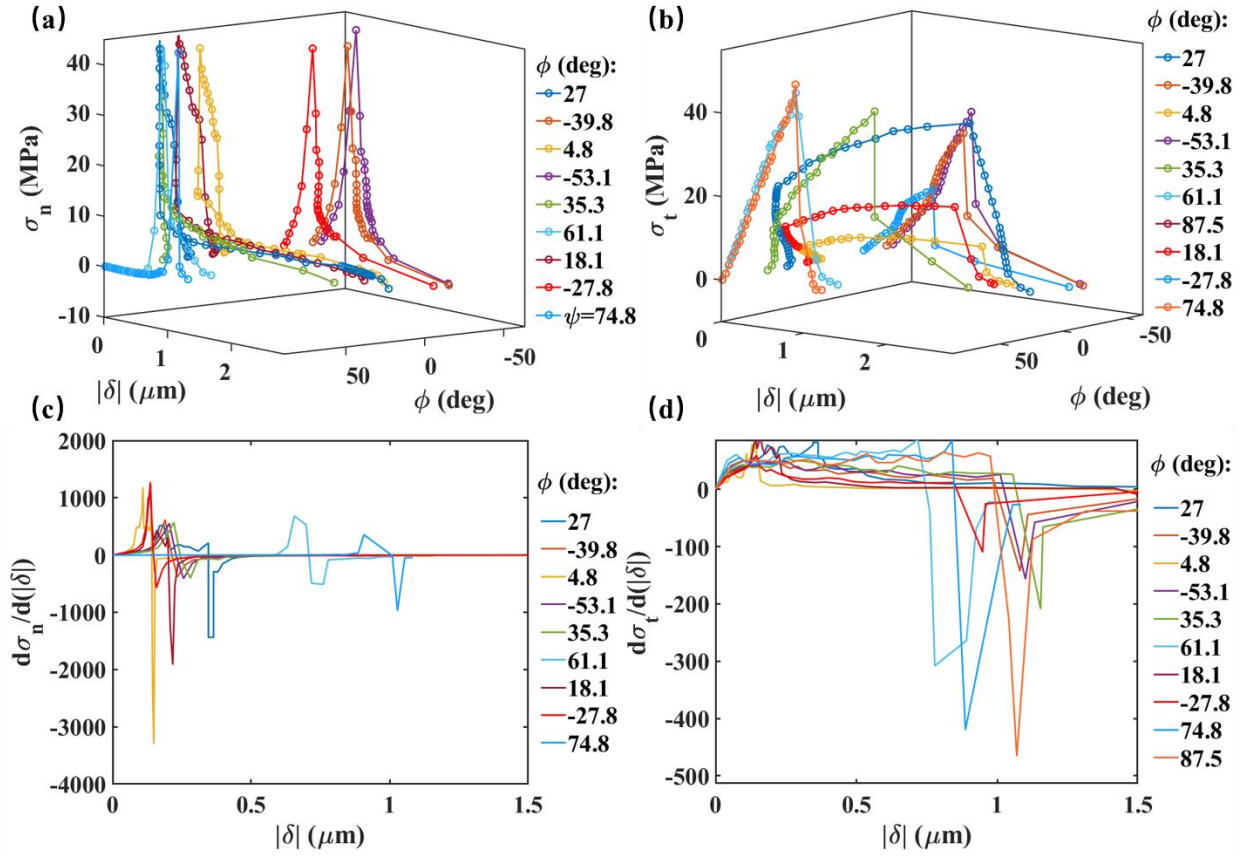


Fig. 2. Experimental data of (a) normal and (b) tangential TSR in terms of total separation and phase angle. Gradient of (c) normal and (d) tangential tractions.

For instance, we explore the fitting of the experimental data with one of the most popular potential based models: the Park, Paulino, and Roesler (PPR) model [29], which offers a large range of flexibility for modeling TSR using eight independent and adjustable parameters. The normalized modeling results are compared with the targeted experimental data in Fig. 3. From these fitting results, we note that the inconsistency is mainly due to the smoothness of the PPR model in contrast with the sharp profile of the experimentally measured TSR. The fitting processes using Monte Carlo algorithms are provided in Section S2 of Supplementary Information. The gradient surfaces and curves along fixed phase angle loading paths are provided in Fig. S1-S2 of Supplementary Information.

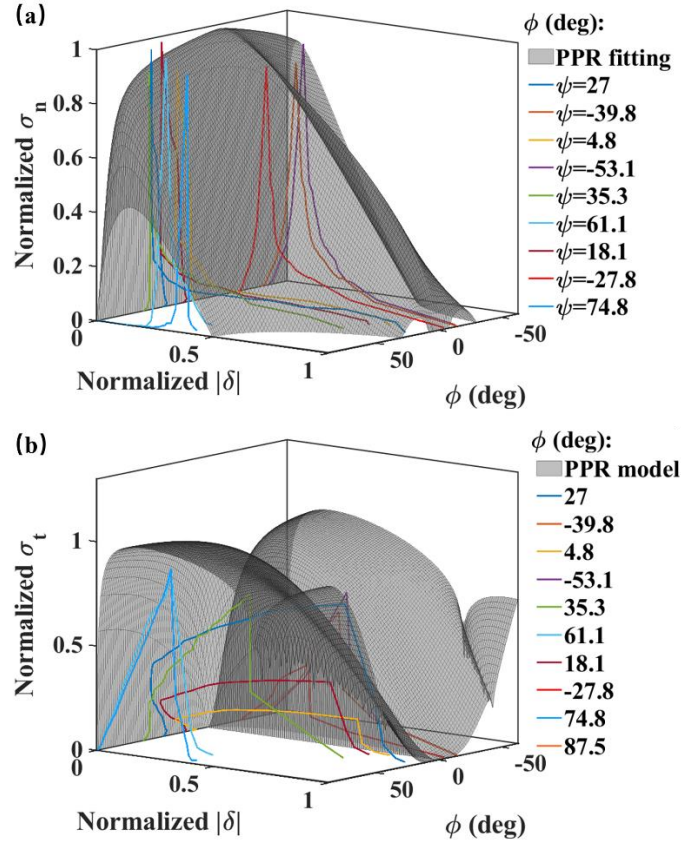


Fig. 3. Normalized (a) normal and (b) tangential traction surfaces fitting using the PPR model.

Certainly, there are other available models which could provide better fitting of the experimental data. However, the authors would argue that these models would suffer the same challenges as the PPR model. This is due to the fundamental conflict between the theoretically conceived modeling approach and the unexpected experimental data. In other words, the smoothness required in the selection of functional form to describe the interfacial energy are often ideal so that it cannot fully capture the richness of the experimental data. Therefore, there is a need for the development of a data-driven model that allows the direct modeling of TSR from the experimental data to preserve the richness in the data sets and simultaneously capture the laws of physics behind these data sets. Here we developed such an approach by combining the deep neural networks (DNN) with the TC conditions.

## 2.2 Thermodynamic consistent (TC) conditions of TSR

We firstly investigated the TC conditions that the experimentally extracted TSR should satisfy, which are: (TC1) the positive energy dissipation condition, (TC2) the local fastest descending condition, and (TC3) the conservative loading path condition. In this section, each of the three TC



conditions are described, quantitatively defined, and prioritized based on data features and observations on experiment phenomena.

### 2.2.1 TC1: Positive energy dissipation condition

The fracture process at interface is a process where the material integrity is progressively lost due to the generation and propagation of material defects, which yield a cracked fracture interface as shown in Fig. 4a. Energy dissipation and the macroscopic material properties are degraded in this process. The degradation degree could be represented with the damage parameter,  $d$ , ranging from 0 to 1, where 1 represents for intact interface and 0 for a totally fracture [30, 31]. For a monotonic loading, the energy dissipation for the interfacial delamination is an irreversible process, i.e., positive energy dissipation, which also implies that the corresponding damage parameter should be monotonically decreasing during the loading process. This TC condition requirement can be therefore formulated as follows.

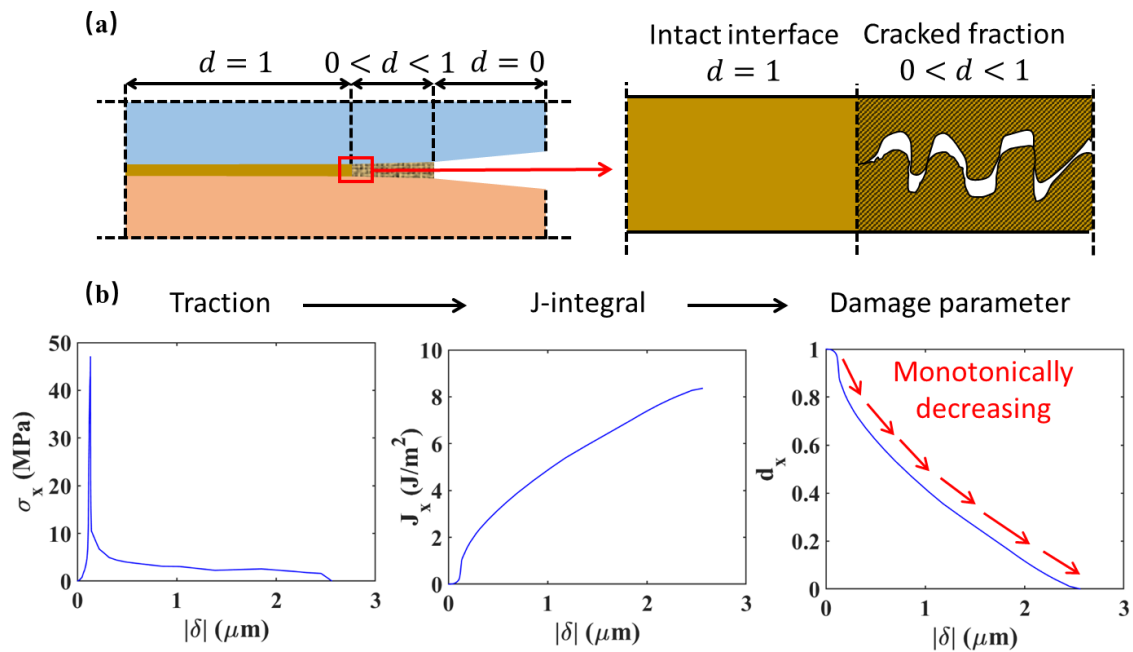


Fig. 4. (a) Damage parameter of an interface. (b) Traction ( $\sigma_x$ , where  $x$  for  $n$  (normal) or  $t$  (tangential)) versus separation norm ( $|\delta|$ ), J-integral ( $J_x$ ) versus  $|\delta|$  and damage parameter ( $d_x$ ) versus  $|\delta|$ .

First, the damage parameters for normal and tangential cases ( $d_n$ ,  $d_t$ ) are defined based on the J-integrals and toughness,

$$d_n(\delta_n) = 1 - \frac{J_n(\delta_n)}{\Gamma_n} \quad (2a)$$

$$d_t(\delta_t) = 1 - \frac{J_t(\delta_t)}{\Gamma_t} \quad (2b)$$

where  $J_n$  and  $J_t$  are the normal and tangential J-integrals obtained by integrating tractions with respect to separations, as defined in following equations:

$$J_n(\delta_n) = \int_0^{x=\delta_n} \sigma_n(x) dx \quad (3a)$$

$$J_t(\delta_t) = \int_0^{x=\delta_t} \sigma_t(x) dx \quad (3b)$$

The positive energy dissipation condition can be fulfilled by enforcing a monotonically decreasing damage parameter and a positive dissipation (Clausius-Duhem inequality) as,

$$1 - \frac{\partial d_n}{\partial \delta_n} = \frac{\partial}{\partial \delta_n} \left( \frac{\int_0^{x=\delta_n} \sigma_n(x) dx}{\Gamma_n} \right) > 0 \quad (4a)$$

$$1 - \frac{\partial d_t}{\partial \delta_t} = \frac{\partial}{\partial \delta_t} \left( \frac{\int_0^{x=\delta_t} \sigma_t(x) dx}{\Gamma_t} \right) > 0 \quad (4b)$$

where  $\Gamma_n = \max(J_n)$ ,  $\Gamma_t = \max(J_t)$  are normal and tangential toughness.

As an example, the traction, J-integral, and damage parameter for an experimentally obtained TSR with a nominal phase angle of  $27^\circ$  are calculated and shown in Fig. 4b. The calculated J-integral increases while the corresponding damage parameter decreases monotonically, indicating that this experimentally obtained TSR follows the monotonic positive energy dissipation condition.

### 2.2.2 TC2: Local fastest descending condition

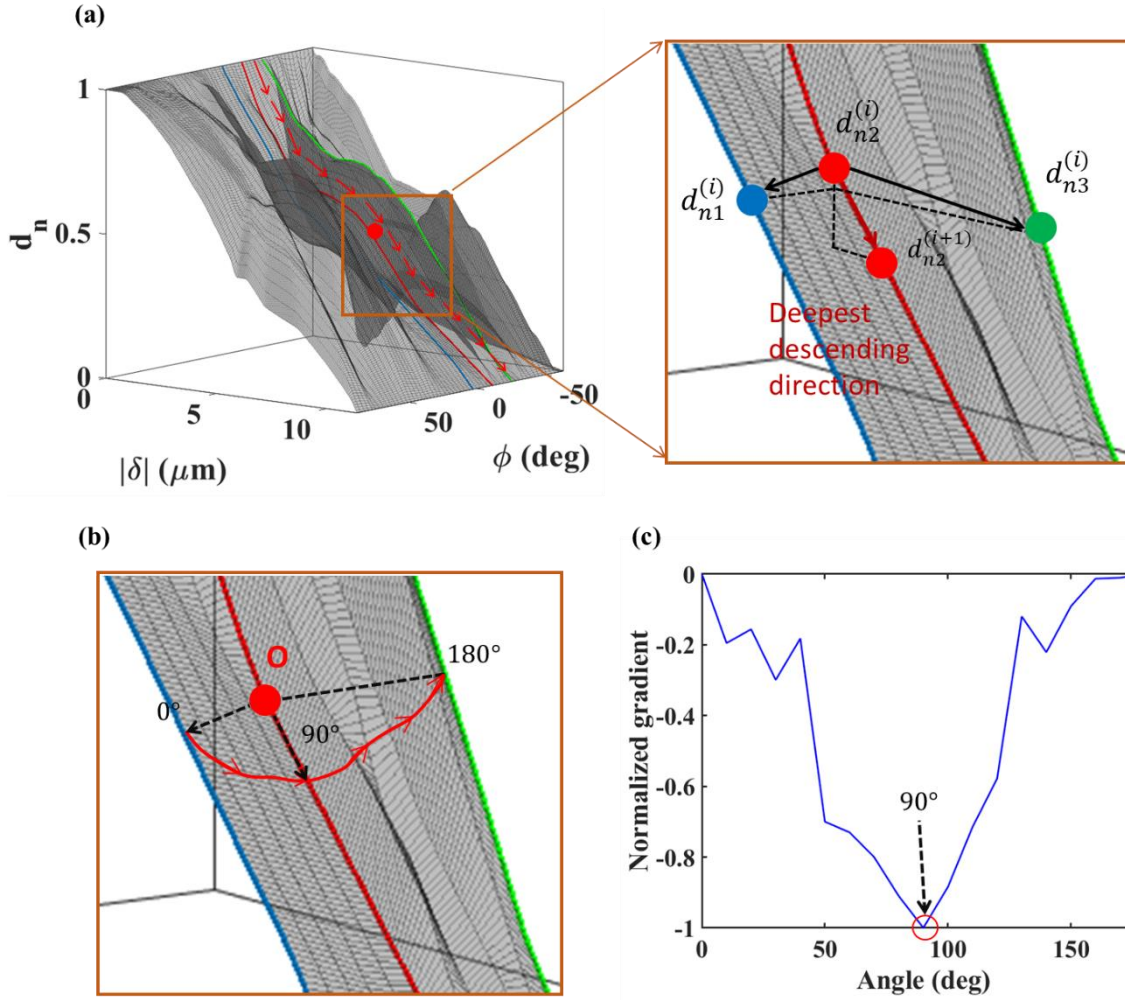


Fig. 5. (a) Illustration of the local deepest descending condition. (b) Illustration and (c) values of normalized gradient for point O along all directions.

In addition to the positive energy dissipation condition, the dissipation rate should reach a local maximum when the interfacial separation reaches a local maximum. For a damage parameter surface shown in Fig. 5a, the loading along fixed phase angle paths results in the largest separation change, thus it is the fastest energy dissipation direction. For the point  $d_{n2}^{(i)}$ , while loading along fixed phase angle path and moving to point  $d_{n2}^{(i+1)}$ , it results in the largest decrease of the damage parameter, comparing with the neighboring points where phase angle is changed, for example,  $d_{n1}^{(i)}$  and  $d_{n3}^{(i)}$ . This local fastest descending condition (TC2 condition) is applied to both normal and tangential cases and can be described with following equations,

$$\left(\frac{\partial d_n}{\partial \delta}\right)_{\phi=\phi_0, \delta=|\delta|} < \left(\frac{\partial d_n}{\partial \delta}\right)_{\phi \neq \phi_0, \delta \neq |\delta|} \quad (5a)$$

$$\left(\frac{\partial d_t}{\partial \delta}\right)_{\phi=\phi_0, \delta=|\delta|} < \left(\frac{\partial d_t}{\partial \delta}\right)_{\phi \neq \phi_0, \delta \neq |\delta|} \quad (5b)$$

Fig. 5b-c shows the gradient change for a point C along all directions. While loading angle changes from  $0^\circ$  to  $180^\circ$ , the gradient decreases until reaching the local minimum at  $90^\circ$ , then increases again until reaching 0 gradient at  $180^\circ$ .

### 2.2.3 TC3: conservative loading path condition

For interfacial failure processes, the total energy dissipation should equal to the summation of the energy dissipation parts along the normal and tangential separation directions if there is no other non-mechanical energy dissipation for the system (i.e., no heat generated from friction). For a mixed-mode TSR along fixed phase angle loading path, the total J-integral ( $J_{total}$ ) is composed with normal and tangential J-integral components, as shown in Fig. 6,

$$J_{total}(\sigma_n, \sigma_t, \delta_n, \delta_t) = J_n(\sigma_n, \delta_n) + J_t(\sigma_t, \delta_t) \quad (6)$$

Under this circumstance, the normal and tangential separations increase proportionally with a ratio that equals the tangential of the phase angle,

$$\frac{\delta_t}{\delta_n} = \tan \phi \quad (7)$$

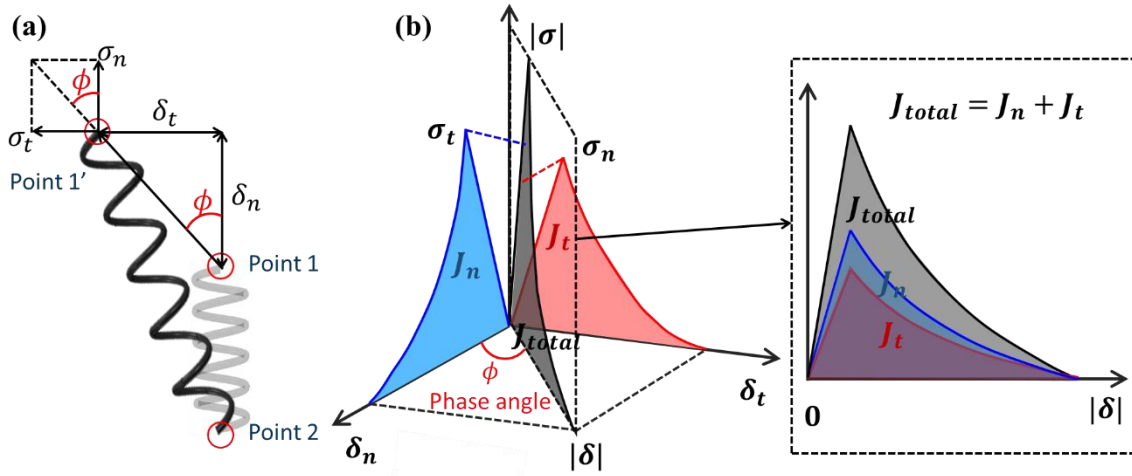


Fig. 6. (a) Normal and tangential tractions and separations. (b) Energy conservation illustration.

By replacing the normal and tangential J-integrals in Eq. 6 with integrations of tractions with respect to separations, the relation between normal and tangential tractions is obtained and expressed as follows:

$$\frac{\sigma_t}{\sigma_n} = \frac{\delta_t}{\delta_n} = \tan \phi \quad (8)$$

The detailed derivation from Eq. 6 to Eq. 8 could be found in Section S3 of Supplementary Information. Eq. 8 is the conservative loading path condition (TC3 condition) followed by the normal and tangential traction surfaces.

In review of all three TC conditions, TC1 and TC2 are extracted or built based on the irreversible nature of the energy dissipation as stated in the second law of thermodynamics, thus are the stronger constraints. TC3 condition is identified based on the assumption that the delamination occurs at the interface without frictional energy dissipation, which may not be true based on some of the experiment observations [32-34]. Therefore, TC3 condition is a relatively weaker condition that needs to be satisfied in comparison with TC1 and TC2 conditions.

### 3. Thermodynamic consistent neural network (TCNN)

We selected the DNN and constructed a data-driven model to predict the TSR surfaces based on experiment data sets. To implement TC conditions into this model, each of the 3 TC conditions (TC1, TC2 and TC3) are embedded as loss function terms of the DNN model to form the TCNN. In addition, the importance of the experimental data and the TC conditions are adjusted based on Bayesian optimization algorithm, to balance the contradictions between experimental data and TC conditions.

#### 3.1 Deep neural network construction

We firstly constructed the DNN with two hidden layers and 60 neurons for each layer as shown in Fig. 7. The inputs are separation norm ( $|\delta|$ ) and phase angle ( $\phi$ ) as defined in Eq. 1a-b, and the outputs are normal and tangential J-integrals ( $J_n, J_t$ ), as shown in Fig. 7.

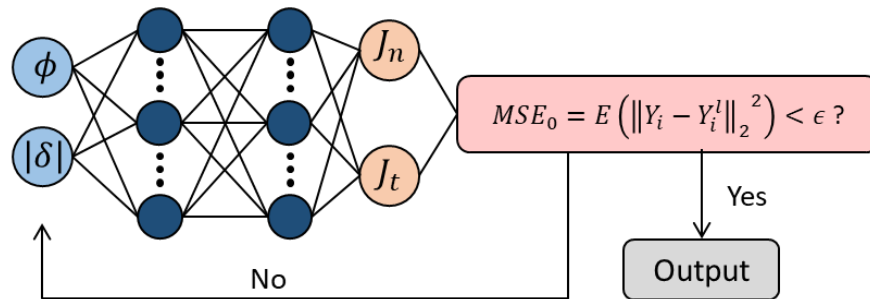


Fig. 7. Deep neural network structure and optimization algorithm.

The input and output data are normalized through a mean of dividing by their maximum values with following equations to eliminate the introduced bias from value discrepancy,

$$X_{norm}^{(i)} = \frac{X^{(i)}}{\max_{i \in [1, n]} X^{(i)}} \quad (9a)$$

$$Y_{norm}^{(i)} = \frac{Y^{(i)}}{\max_{i \in [1, n]} Y^{(i)}} \quad (9a)$$

where  $X^{(i)}$  and  $Y^{(i)}$  stand for the  $i$ th point of the input and output data sets, and  $n$  is the number of the dataset,  $X_{norm}^{(i)}$  and  $Y_{norm}^{(i)}$  are the normalized data for DNN training. We use the hyperbolic tangent (tanh) function as the nonlinear activation function and Adam optimizer that has been widely used as an effective and fast optimization method. The objective is to minimize the loss function that is the expectation of mean squared error (MSE), which is defined as:

$$MSE_0 = E \left( \|Y_i - Y_i^l\|_2^2 \right) \quad (10)$$

where  $Y_i$  and  $Y_i^l$  are  $i$ th point of true output and predicted output. Operator  $\|\cdot\|$  represents the 2-dimensional Euclidean ( $l_2$ ) norm. The training process is completed when 1,000,000 training epochs are reached, or the loss function value is smaller than a specific threshold  $\epsilon = 10^{-3}$ . Then we can use this neural network model to predict the J-integral surfaces.

### 3.2 Implementation of TC conditions in TCNN

TC conditions are added to loss function as a penalty term for effective and accurate learning of the TSR. For DNN models, the training process is one that searches for a solution that fits well with the training data sets. The loss function, where MSE is adopted for DNN models, is used to justify how well this fitting is and then adopted in optimization algorithms for next step training. By implementing the TC conditions as loss function terms, the trained models violating the TC conditions are ‘punished’ and the ‘survived’ models are more compliant to TC conditions. This concept has been implemented in physics informed (or guided) neural networks and worked well in applications [35-37].

In our work, each of the three TC conditions are imposed on 10 loading paths with fixed phase angle ranging from  $-60^\circ$  to  $90^\circ$ , shown as red lines in Fig. 8, identical intervals of  $15^\circ$  are used for each two neighboring paths. The interval along  $|\delta|$  coordinate is set as  $0.1 \mu\text{m}$  within a range of  $[0, 3 \mu\text{m}]$ . We refer to these paths as constraining paths, to differentiate from the experimental paths. For each iteration, along each constraining path, the loss function value is calculated

automatically based on predicted J-integral surfaces. This value is then used to adjust the TCNN and move on to next iteration.

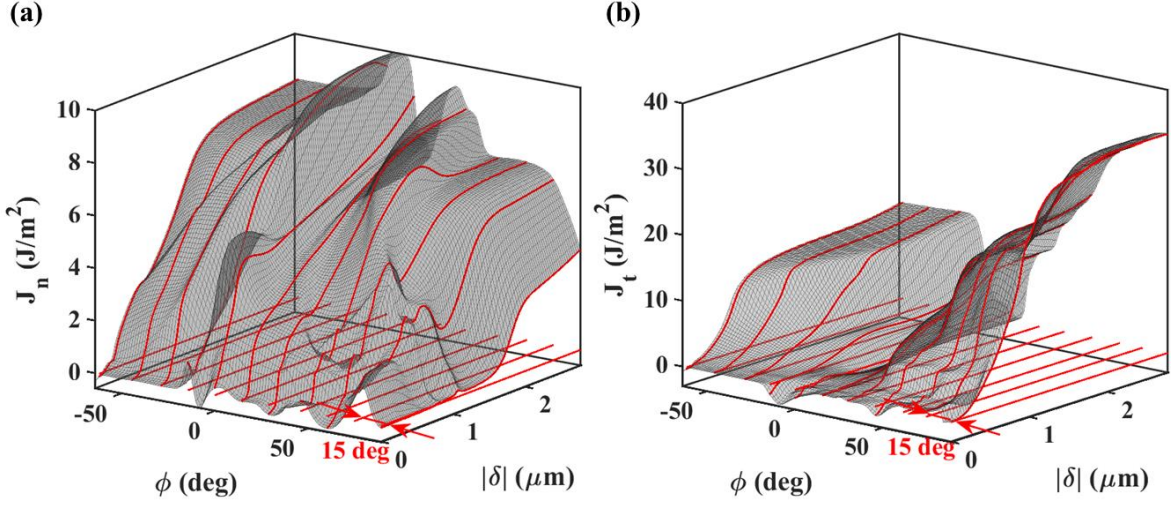


Fig. 8. (a-b) Illustration of fixed phase angle constraining paths on normal and tangential J-integrals.

### 3.2.1 Implementation of TC1

TC1 is imposed on constraining paths on both the normal and tangential output J-integral surfaces. For each training epoch, the gradient of the damage parameter for each constraining path is calculated. Max function is used to compare these values with 0 so that only the positive part, which is contradicting to the TC1 condition,

$$MSE_{1n}^{(j)} = \max\left(\frac{\partial d_n}{\partial \delta_n}, 0\right) = \max_{i \in [1, n-1]} \left(\frac{d_n^{(i+1)} - d_n^{(i)}}{\delta_n^{(i+1)} - \delta_n^{(i)}}, 0\right) \quad (11a)$$

$$MSE_{1t}^{(j)} = \max\left(\frac{\partial d_t}{\partial \delta_t}, 0\right) = \max_{i \in [1, n-1]} \left(\frac{d_t^{(i+1)} - d_t^{(i)}}{\delta_t^{(i+1)} - \delta_t^{(i)}}, 0\right) \quad (11b)$$

where  $d_n^{(i)}$ ,  $d_t^{(i)}$  and  $\delta_n^{(i)}$ ,  $\delta_t^{(i)}$  are the  $i$ th normal and tangential damage parameters as well as separations on  $j$ th constraining path.  $MSE_{1n}^{(j)}$  and  $MSE_{1t}^{(j)}$  are the normal and tangential components related to  $j$ th constraining path.  $n$  is the total number of samples for each constraining path. Assuming normal and tangential damage parameter with equal important weights, the new loss function ( $MSE_1$ ) incorporating TC1 constraint is formulated as,

$$MSE_1 = \frac{1}{2m} \sum_{j=1}^m \left(MSE_{1n}^{(j)} + MSE_{1t}^{(j)}\right) \quad (12)$$

where  $m$  is the number of constraining path. This loss function is averaged over the total number of points on the constraining paths.

### 3.2.2 Implementation of TC2

TC2 condition shown in Eq. 5 constrains the gradient vector direction along the fixed phase angle loading paths. Numerically, this condition is reflected as smaller gradient along  $|\delta|$  dimension while comparing with that along  $\phi$  dimension. Along each constraining path, the difference between gradients along  $|\delta|$  and  $\phi$  dimensions are calculated and compared with value 0 using max functions, which is formulated as,

$$MSE_{2n}^{(i,j)} = \max_{\substack{i \in [1, n-1] \\ j \in [2, m-1]}} \left( \frac{\partial d_n^{(i,j)}}{\partial (|\delta|)} - \frac{\partial d_n^{(i,j)}}{\partial \phi}, 0 \right) = \max_{\substack{i \in [1, n-1] \\ j \in [2, m-1]}} \left( \left( \frac{d_n^{(i,j)} - d_n^{(i+1,j)}}{\delta_n^{(i+1,j)} - \delta_n^{(i,j)}} \right) - \left( \frac{d_n^{(i,j)} - d_n^{(i,j+1)}}{\phi^{(i,j+1)} - \phi^{(i,j)}} \right), 0 \right) + \max_{\substack{i \in [1, n-1] \\ j \in [2, m-1]}} \left( \left( \frac{d_n^{(i,j)} - d_n^{(i+1,j)}}{\delta_n^{(i+1,j)} - \delta_n^{(i,j)}} \right) - \left( \frac{d_n^{(i,j)} - d_n^{(i,j-1)}}{\phi^{(i,j)} - \phi^{(i,j-1)}} \right), 0 \right) \quad (13a)$$

$$MSE_{2t}^{(i,j)} = \max_{\substack{i \in [1, n-1] \\ j \in [2, m-1]}} \left( \frac{\partial d_t^{(i,j)}}{\partial (|\delta|)} - \frac{\partial d_t^{(i,j)}}{\partial \phi}, 0 \right) = \max_{\substack{i \in [1, n-1] \\ j \in [2, m-1]}} \left( \left( \frac{d_t^{(i,j)} - d_t^{(i+1,j)}}{\delta_t^{(i+1,j)} - \delta_t^{(i,j)}} \right) - \left( \frac{d_t^{(i,j)} - d_t^{(i,j+1)}}{\phi^{(i,j+1)} - \phi^{(i,j)}} \right), 0 \right) + \max_{\substack{i \in [1, n-1] \\ j \in [2, m-1]}} \left( \left( \frac{d_t^{(i,j)} - d_t^{(i+1,j)}}{\delta_t^{(i+1,j)} - \delta_t^{(i,j)}} \right) - \left( \frac{d_t^{(i,j)} - d_t^{(i,j-1)}}{\phi^{(i,j)} - \phi^{(i,j-1)}} \right), 0 \right) \quad (13b)$$

where  $d_n^{(i,j)}$ ,  $d_t^{(i,j)}$  and  $\delta_n^{(i,j)}$ ,  $\delta_t^{(i,j)}$  are the  $i$ th normal and tangential damage parameters as well as separations on  $j$ th constraining path.  $MSE_{2n}^{(i,j)}$  and  $MSE_{2t}^{(i,j)}$  are the normal and tangential components related to  $i$ th point on  $j$ th constraining path of this loss function term.

For data points obeying the TC2 condition, this difference is negative and the corresponding loss function term yields 0. For contradicting data points, the loss function term equals to the positive difference value and is minimized during the training process.

These TC2 constraints are imposed separately on normal and tangential J-integral surfaces and play an equally important role on the total loss function term ( $MSE_2$ ),

$$MSE_2 = \frac{1}{2mn} \left( \sum_{i=1}^{n-1} \sum_{j=2}^{m-1} MSE_{2n}^{(i,j)} + \sum_{i=1}^{n-1} \sum_{j=2}^{m-1} MSE_{2t}^{(i,j)} \right) \quad (14)$$

### 3.2.3 Implementation of TC3

TC3 condition confines the ratio between normal and tangential tractions along the constraining paths. The loss function term ( $MSE_3$ ) for each constraining path is defined with following equation,



$$MSE_3^{(j)} = \frac{1}{n} \sum_{i=1}^n \left| \left( \frac{\sigma_t^{(i,j)}}{\sigma_n^{(i,j)}} - \tan(\phi^{(j)}) \right) \right| \quad (15)$$

The  $\sigma_n^{(i,j)}$ ,  $\sigma_t^{(i,j)}$  are the  $i$ th normal and tangential tractions of  $j$ th constraining path.  $MSE_3^{(j)}$  is the loss function related to the  $j$ th constraining path. Different from the TC1 and TC2 constraints that are inequality constraints, TC3 constraint condition is an equality constraint.

The assembled total loss function ( $MSE_3$ ) term corresponding to the TC3 constraint is written by,

$$MSE_3 = \frac{1}{m} \sum_{j=1}^m MSE_3^{(j)} \quad (16)$$

### 3.2.4 Weighted loss function of TCNN

Loss function terms with TC1-TC3 constraints, as defined in Eq. 12, 14, 16 respectively, are implemented to a DNN so as to construct a TCNN. Schematic for this TCNN is shown in Fig. 9. The DNN models use the same architecture as discussed in Section 3.1, that is two hidden layers with 60 neurons for each hidden layer.

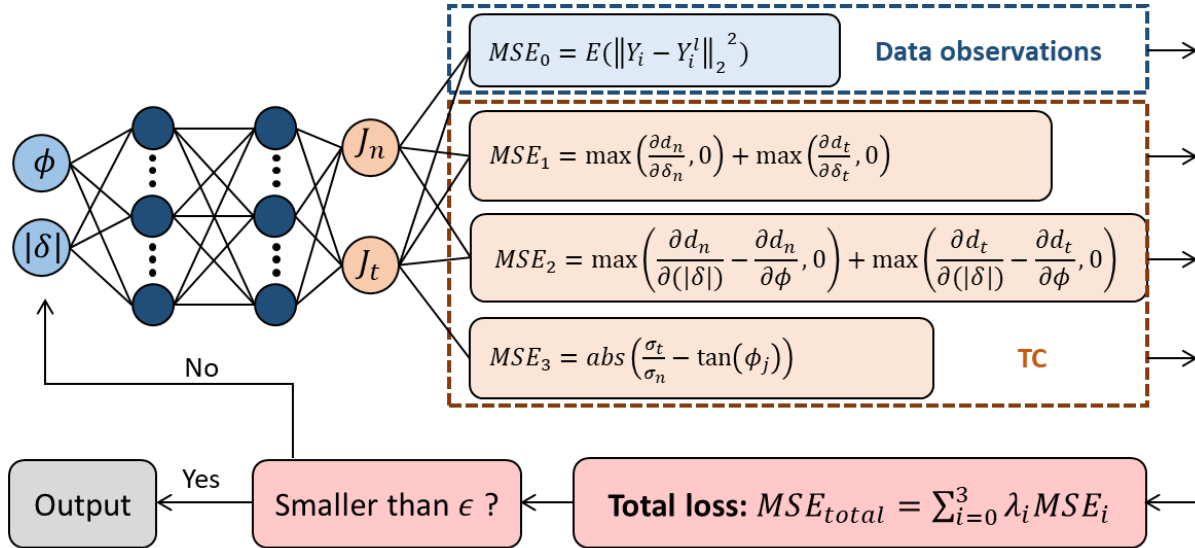


Fig. 9. Schematic of a thermodynamic consistent neural network (TCNN) for solving TSR problems.

The goal of this objective is to minimize the total loss function,  $MSE_{total}$ , which is defined as weighted summation of loss function corresponding to MSE ( $MSE_0$ ) that is from the data observations and TC constraints ( $MSE_1 - MSE_3$ ) separately,

$$MSE_{total} = \sum_{i=0}^3 \lambda_i MSE_i \quad (17)$$

where  $\lambda_i, i = 0, 1, 2, 3$  are the weighting factors for each of the loss function penalized terms.

To investigate the effect of imposed TC constraints on prediction performance, we change the relative important weights  $\lambda_i$  on the overall loss function. 3 TCNN models with different constraints are investigated and named as TCNN-set1 to TCNN-set3. The evolved constraints and weighting factors for all sets are listed in Table. 1, where the summation of  $\lambda_0 - \lambda_3$  equals 1.0.

Table. 1 Weighting factor setting

	$\lambda_0$	$\lambda_1$	$\lambda_2$	$\lambda_3$	Active TC constraints
TCNN-set1	0.800	0.200	0.000	0.000	TC1
TCNN-set2	0.600	0.200	0.200	0.000	TC1, TC2
TCNN-set3	0.570	0.200	0.200	0.0300	TC1, TC2, TC3

From TCNN-set1 to TCNN-set3, the weighting factor for MSE term ( $\lambda_0$ ) is reduced and redistributed to TC1-TC3 conditions step by step. For all TCNN sets, an accurate fitting to the experimental TSRs along experiment paths is still treated with highest priority. Correspondingly, the  $\lambda_0$  is kept above 0.5 to ensure main features are captured from the experimental data. TC1 and TC2 constraints are treated with equal importance and thus have the same weighting factor. Compared with inequality constraints in TC1 and TC2 constraints, TC3 constraint is a stronger equality constraint that can contribute to the best part of the loss function value when assigned with same weighting factor. In this manner, the training process will satisfy this TC3 constraint with first priority and thus weaken the constraining effects of inequality constraints. Here we assign  $\lambda_3$  with a relatively smaller value to balance the contribution from the three TC conditions.

### 3.3 Bayesian optimization

Bayesian optimization (BO) is used to automatically adjust the weighting factors, so that the relative importance of MSE and TC conditions are optimized, and a minimum total loss function can be reached.

In many cases, experimental data is companied with system errors and noises, which can lead to local conflictions between experimental results and TC conditions. When used as training data sets in TCNN models, these interferences could significantly affect the predicted traction surfaces and lead to TC condition violating regions. Moreover, this conflict between experimental data and TC conditions can cause problems to the TCNN training processes, such as excessive training to converge and poor fitting of experimental data. By using the automatic weighting factor adjustment algorithms for optimization, a minimum loss function value can be reached with

optimized weighting factors. In this manner, the TSR prediction could ‘bend’ the part of experimental data to fit with TC conditions when conflicts are found while still capturing the global main feature of the experimental data.

BO algorithm, which performs global minimization of unknown functions with multiple degree of freedoms, is adopted for the optimization. Using knowledge of some prior sampling over the space of this unknown function, BO algorithm estimates the areas with highest possibility to generate most promising results. In this way, instead of conducting random search or grid search where results should be obtained for every set of parameters, the BO algorithm provides a more optimal searching scheme and reduces the number of trial attempts by taking advantage of prior knowledge and the calculated likelihood of the unknown area. The implementation is conducted within the TuRBO algorithm, which solves for global optimization of large-scale high-dimensional problems using local probabilistic approach [25].

Based on TCNN model and the BO algorithm, the set of the weighting factors are determined to minimize the overall loss function value while following actions are conducted: (1) the weighting factors for all terms in loss function are loosened up and allowed to vary within a reasonable range; (2) The upper bound of the range for the weighting factor associated with the MSE is set to be lower than the value used in TCNN-set3 model.

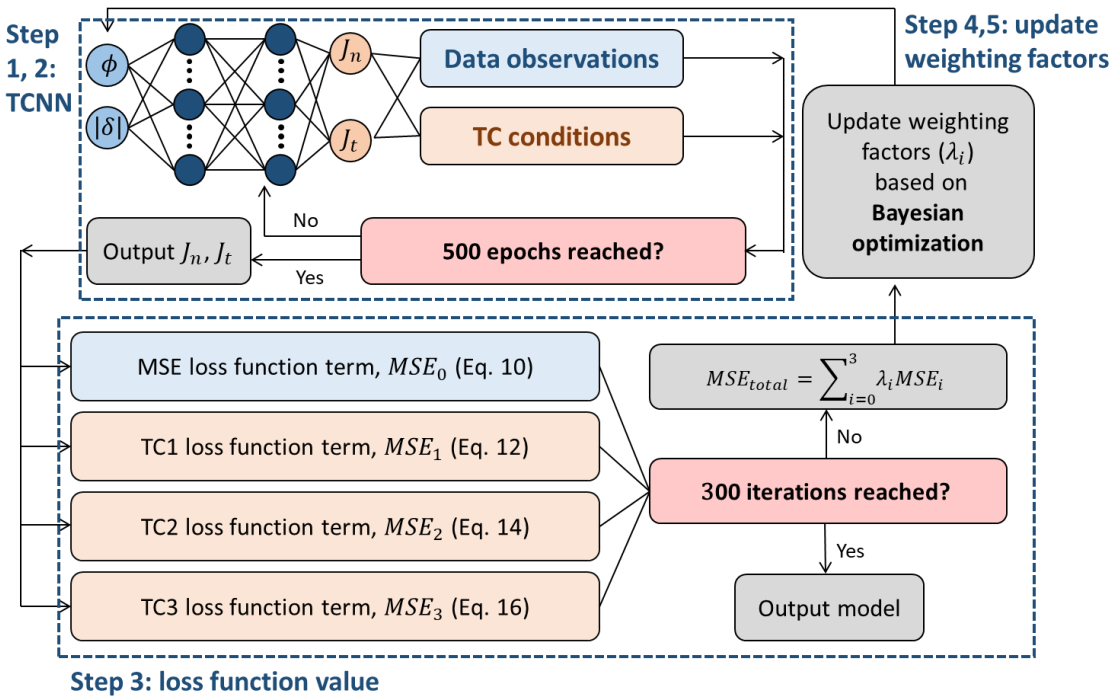


Fig. 10. Weighting factor optimization with BO algorithms.

The implementation of TCNN framework with BO algorithm is shown in Fig. 10 with following steps.

Step 1. The normalized training data and the randomly initiated weighting factor are input for the first step TCNN training.

Step 2. TCNN is trained for 500 epochs, this relatively low epoch number is to reduce the time required for each BO optimization iteration.

Step 3. Upon the completion of the TCNN training process, values of loss function terms corresponding to MSE (based on Eq. 10) and TC1-3 conditions (based on Eq. 12, Eq. 14 and Eq. 16) are calculated. The total loss function value is then obtained with Eq. 17.

Step 4. The weighting factors is updated based on BO criterions.

Step 5. The updated weighting factors are input to the TCNN to start next iteration. This cycle continues until the maximum budget (300 iterations) is reached.

For each iteration in the BO algorithm, the weighting factors are optimized under two constraints: (1) each weighting factor varies within a range defined with a lower and upper bound ( $\lambda_i \in [\lambda_i^{lower}, \lambda_i^{upper}]$ ,  $i = 0, 1, 2$  or  $3$ ). This allows the user to determine which constraint has higher importance while avoiding the weighting factors smaller than zero. (2) Summation of all the weighting factors equals to 1, or  $\sum_{i=0}^3 \lambda_i = 1$ . The updated weighting factor set is transferred into the TCNN for next step training. The end of the optimization process is reached when the certain maximum number (e.g., 300) of iteration is reached.

#### **4. Mixed-mode TSR modeling results**

To demonstrate the effectiveness of the TCNN framework, we firstly modeled the mixed-mode TSR using a DNN model without any constraints. Subsequently, we demonstrate the superior performance of TCNN and TCNN with BO algorithm.

##### **4.1 Modeling using DNN**

The modeled normal and tangential J-integral surfaces are illustrated with respect to  $|\delta|$  and  $\phi$  as shown in Fig. 11a-b. The modeling results along experiment loading paths are extracted and compared with experimental data sets. As shown in Fig. 11c-d. It shows that the modeling results using trained NN fit well to the experimental data along experiment loading paths.

We then evaluated how well this model satisfies the TC conditions. Based on predicted J-integral surfaces with TCNN models, violations to each of the 3 TC conditions are calculated separately with following approaches and shown in Fig. 11e.

For TC1 condition, the violation ( $\text{Vio}_1$ ) represents for a negative energy dissipation and calculated based on gradient of J-integral predictions using following equation,

$$\text{Vio}_1 = \left| \min \left( \frac{\partial J_n}{\partial |\delta|}, 0 \right) \right| + \left| \min \left( \frac{\partial J_t}{\partial |\delta|}, 0 \right) \right| \quad (18)$$

With this equation, violating data points with negative J-integral gradient are located and their normalized values ( $\text{Vio}_{1,\text{norm}}$ , with respect to maximum value as shown in following equation) are illustrated as red contour in Fig. 11e.

$$\text{Vio}_{1,\text{norm}} = \frac{\text{Vio}_1}{\max(\text{Vio}_1)} \quad (19)$$

For TC2 condition, the predicted J-integrals are firstly transferred to damage surfaces. The gradient change is then calculated with respect to angles for each point as shown in Fig. 5b,c, data points with maximum gradient decrease not along  $90^\circ$  direction are located and the violation ( $\text{Vio}_1$ ) is calculated as the difference between the fastest descending direction and  $90^\circ$ , as shown in following equation.

$$\text{Vio}_2 = |\theta_{ddn} - 90| + |\theta_{ddt} - 90| \quad (20)$$

where  $\theta_{ddn}$  and  $\theta_{ddt}$  are the angle of fastest descending direction for the point in normal and tangential J-integral surfaces. Normalized value ( $\text{Vio}_{2,\text{norm}}$ , with respect to maximum value as shown in following equation) is shown as blue contour in Fig. 11e.

$$\text{Vio}_{2,\text{norm}} = \frac{\text{Vio}_2}{\max(\text{Vio}_2)} \quad (21)$$

For TC3 condition, the ratio between normal and tangential tractions ( $\sigma_n, \sigma_t$ ) are calculated and compared with the tangent of phase angle,  $\phi$ . Noting that exact equivalence is mostly impossible, we use a threshold angle ( $\epsilon_{phi}$ ) of  $5^\circ$  and the violation ( $\text{Vio}_3$ ) is reached when the difference between the ratio and the phase angle tangent is larger than  $\epsilon_{phi}$ :

$$\text{Vio}_3 = \max \left( \left| \frac{\sigma_t}{\sigma_n} - \tan \phi \right|, \tan(\epsilon_{phi}) \right) - \tan(\epsilon_{phi}) \quad (22)$$

Also, the normalized value ( $\text{Vio}_{3,\text{norm}}$ ) is used and depicted as green contour shown in Fig. 11e.

$$\text{Vio}_{3,\text{norm}} = \frac{\text{Vio}_3}{\max(\text{Vio}_3)} \quad (23)$$

Observing from Fig. 11e, the total violation regions combining all 3 TC conditions covers the best part of the modeling region, including both regions covered or not covered by experiment data sets. Overlapping among violation regions for different TC conditions is observed. These results

show that a data driven model like DNN could truthfully learn from the experiment data sets and yield accurate predictions for regions covered by the training data sets. However, for regions with data missing, the NN model cannot predict TSR that follows physics laws.

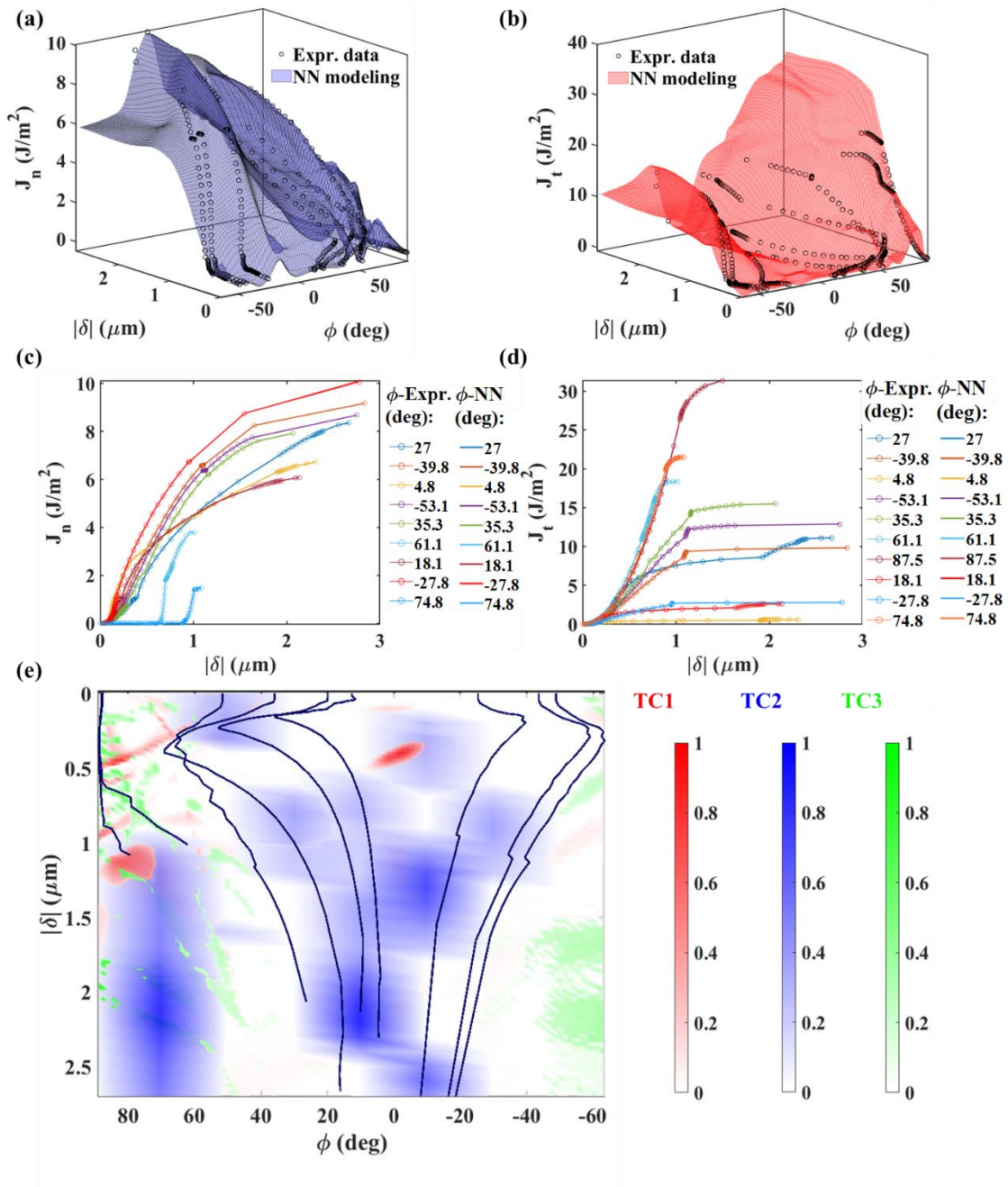


Fig. 11. (a-b) Modeled normal and tangential J-integral surfaces using DNN. (c-d) Modeling results for normal and tangential J-integrals comparing with experiment results. (e) Violation against each of the 3 TC conditions. The red contour shows violation against TC1 condition, blue

contour for TC2 condition and green contour for TC3 condition. Black lines are experiment loading paths.

## **4.2 Modeling using TCNN**

TCNN modeling results comparison with experiment results and violations to TC1-TC3 conditions are shown in Fig. 12-14. Different TC constraint combinations are considered by assigning different weighting factors on the loss function as shown in Tab. 1, where each of modeling results showed in Fig. 12-14 follows the weighting factor settings of TCNN-set1 to TCNN-set3.

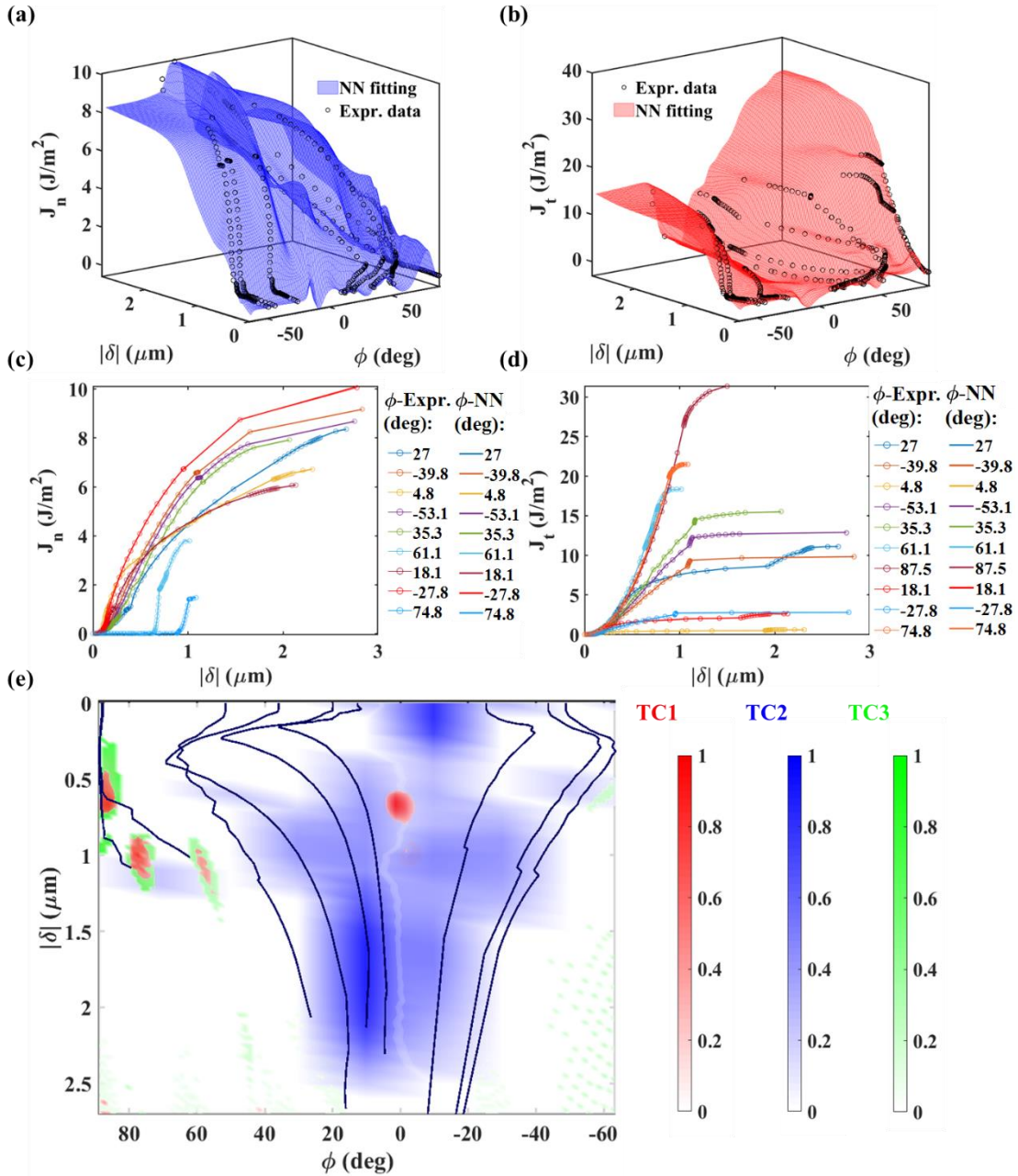


Fig. 12. (a-b) Modeled normal and tangential J-integral surfaces using TCNN with MSE and TC1 constraint (TCNN-set1). (c-d) Modeling results for normal and tangential J-integrals comparing with experiment results. (e) Violation against each of the 3 TC conditions. The red contour shows violation against TC1 condition, blue contour for TC2 condition and green contour for TC3 condition. Black lines are experiment loading paths.



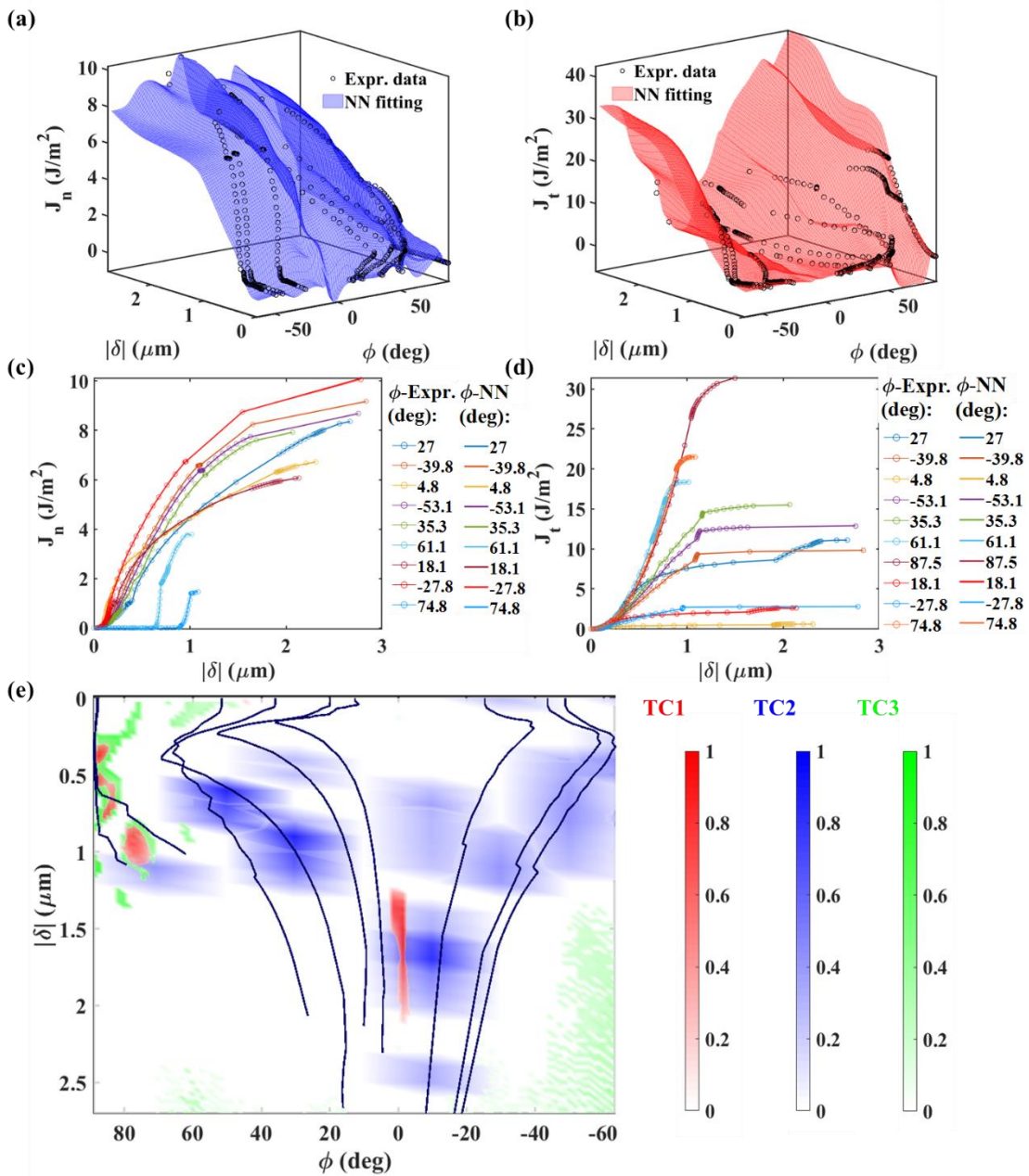


Fig. 13. (a-b) Modeled normal and tangential J-integral surfaces using TCNN with MSE and TC1, TC2 constraints (TCNN-set2). (c-d) Modeling results for normal and tangential J-integrals comparing with experiment results. (e) Violation against each of the 3 TC conditions. The red contour shows violation against TC1 condition, blue contour for TC2 condition and green contour for TC3 condition. Black lines are experiment loading paths.

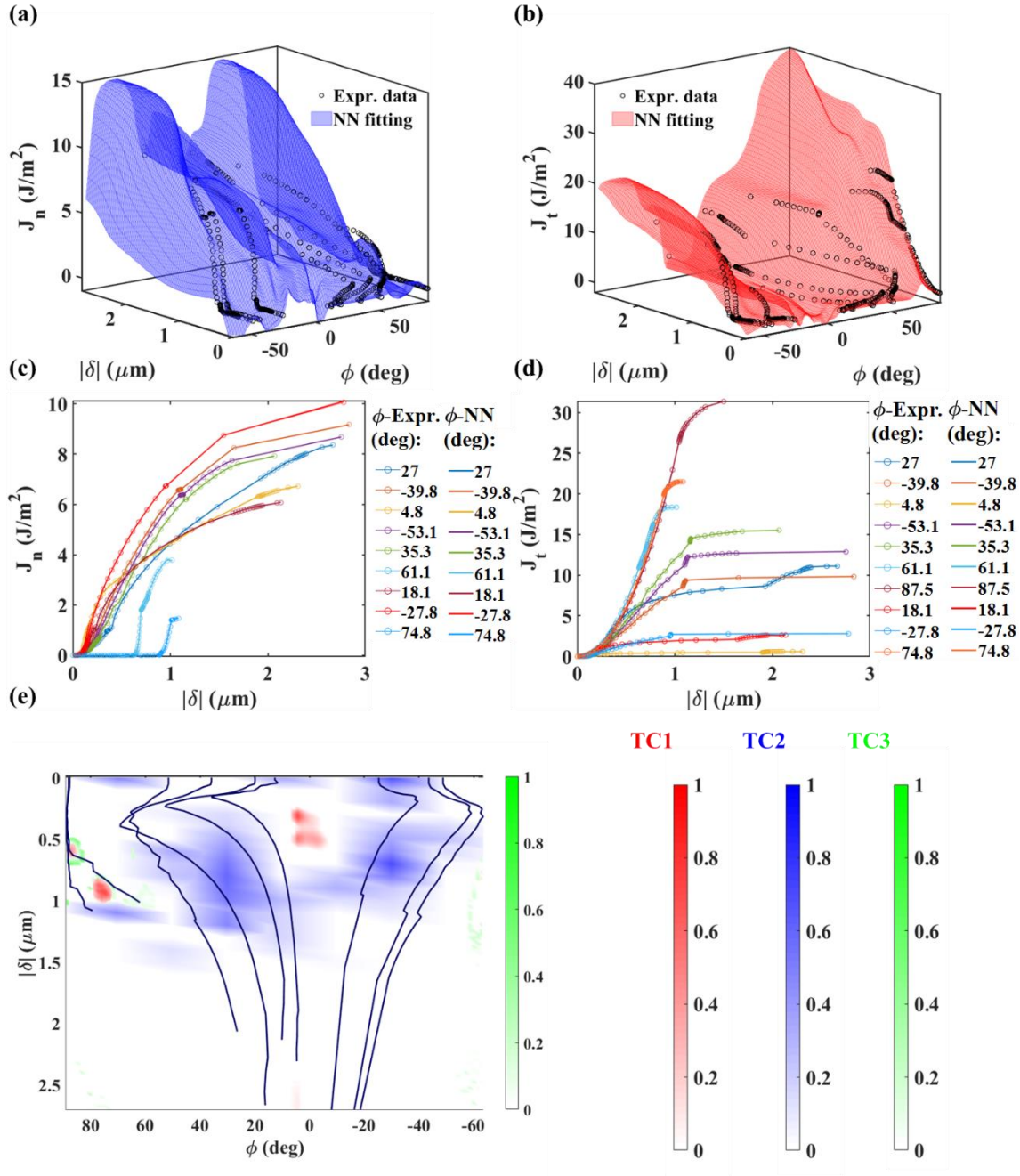


Fig. 14. (a-b) Modeled normal and tangential J-integral surfaces using TCNN with MSE and TC1, TC2, TC3 constraints (TCNN-set3). (c-d) Modeling results for normal and tangential J-integrals comparing with experiment results. (e) Violation against each of the 3 TC conditions. The red contour shows violation against TC1 condition, blue contour for TC2 condition and green contour for TC3 condition. Black lines are experiment loading paths.

Observing from the comparison between modeling results and experimental data as in c-d sub-images of Fig. 12-14, J-integral predictions of all TCNN with different combination of TC constraints fit well with experimental results. This ensures that main features are captured from the experimental data sets during the training progress.

While each of the TC constraints are embedded in the TCNN, the violation regions against the corresponding TC conditions are reduced compared with the modeling results with a simple NN, as shown in e sub-images of Fig. 12-14. It is also observed that when TC constraints are applied, larger overlapping areas exist between the violation regions against different TC conditions, comparing with NN results. For example, violation regions against TC1 condition is almost fully covered by that for TC2 and TC3 conditions as shown in Fig. 13-14e. This further reduces the area of the total violation region. Also, for all TCNN modeling results, the best part of the violation regions is crossed by the experiment loading paths. This proves the existence of the system errors and noises within experimental data, and this leads to a fact that the total violation region for TCNN-set3 has only limited improvement comparing with TCNN-set2, where only TC1 and TC2 constraints are imposed.

### **4.3 Modeling using TCNN with BO optimized weighting factors**

Based on the BO algorithm proposed in Section 3.3, the weighting factors for loss function terms corresponding to MSE and TC1-TC3 constraints are optimized, the convergence for BO process is shown in Fig. 15. 300 iterations are conducted. Loss function value decreases rapidly at the beginning stage and then reduces to around 1.0 within 25 iterations. The decreasing of loss function value for following iterations uses a quasi-exponential form, small fluctuations are found before it reaches the maximum number of iterations. Ranges for each of the 4 weighting factors ( $\lambda_0 - \lambda_3$ ) and optimized values are presented in Tab. 2.

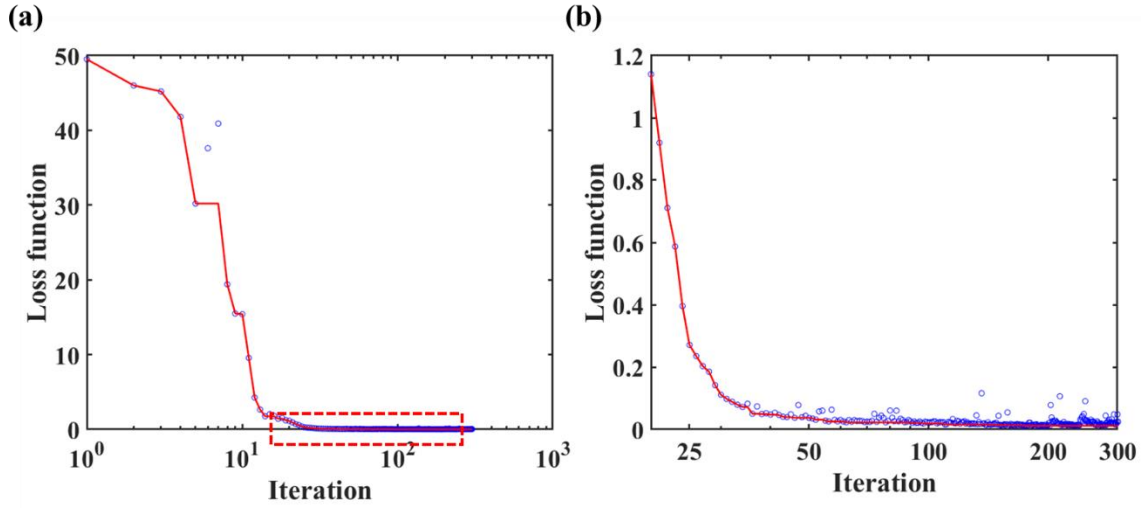


Fig. 15. (a) Convergence of Bayesian optimization process for weighting factors optimization. (b) zoom in image Enlarged image for region within the red frame of (a).

Table. 2 Weighting factors optimization

	Upper bound	Lower bound	Optimized
$\lambda_0$ (MSE)	0.750	0.400	0.519
$\lambda_1$ (TC1)	$(1 - \lambda_0) \times 0.900$	$(1 - \lambda_0) \times 0.100$	0.385
$\lambda_2$ (TC2)	$(1 - \lambda_0 - \lambda_1) \times 0.900$	$(1 - \lambda_0 - \lambda_1) \times 0.100$	0.0622
$\lambda_3$ (TC3)	NA	NA	0.0338

As shown in Tab.2, the fitting to the experimental data is still treated with largest importance. Following is the TC1 condition, which is based on the second law of thermodynamics and obeyed by all experimental data sets. It is surprisingly observed that the TC2 condition is treated with a relatively lower importance when compared with our TCNN-set3 settings (0.0622 comparing to 0.2). One possible explanation is that more energy dissipation mechanisms, friction for example, may be evolved when loading directions are changed. This also reflects as larger blue area in Fig. 12-14e. The optimized weighting factor of TC3 condition is close to our TCNN-set3 settings and keeps as the lowest importance.

Based on the TCNN with optimized weighting factors, modeled J-integral surfaces, modeling results comparison with experiment results and violations to TC1-TC3 conditions are shown in Fig. 16a-b.

Seen from Fig. 16c-d, the modeling results still have a good correspondence with the experimental data while the corresponding weighting factor reduced from 0.570 to 0.519.

Comparing with Fig. 14e, although both cases are applied with 3 TC constraints, the total violation region area in Fig. 16e is reduced by using TCNN modeling results with BO optimized weighting factors. Furthermore, instead of crowding around the experimental data covered regions, smaller violation regions are found to be scattered in different parts of the modeling region. This proves that the confliction between the experimental data and the TC conditions is mediated by the BO optimization progress, a balance is reached by adjusting the weighting factors, where the trend of the experimental data is still fully captured, and the local confliction data points are bypassed to fulfill the TC conditions.

Due to the fact that TC3 condition has the least importance of all 3 TC conditions, BO treats TC3 condition with low priority and the confidence of this condition is sacrificed to reach a better overall TCNN performance.

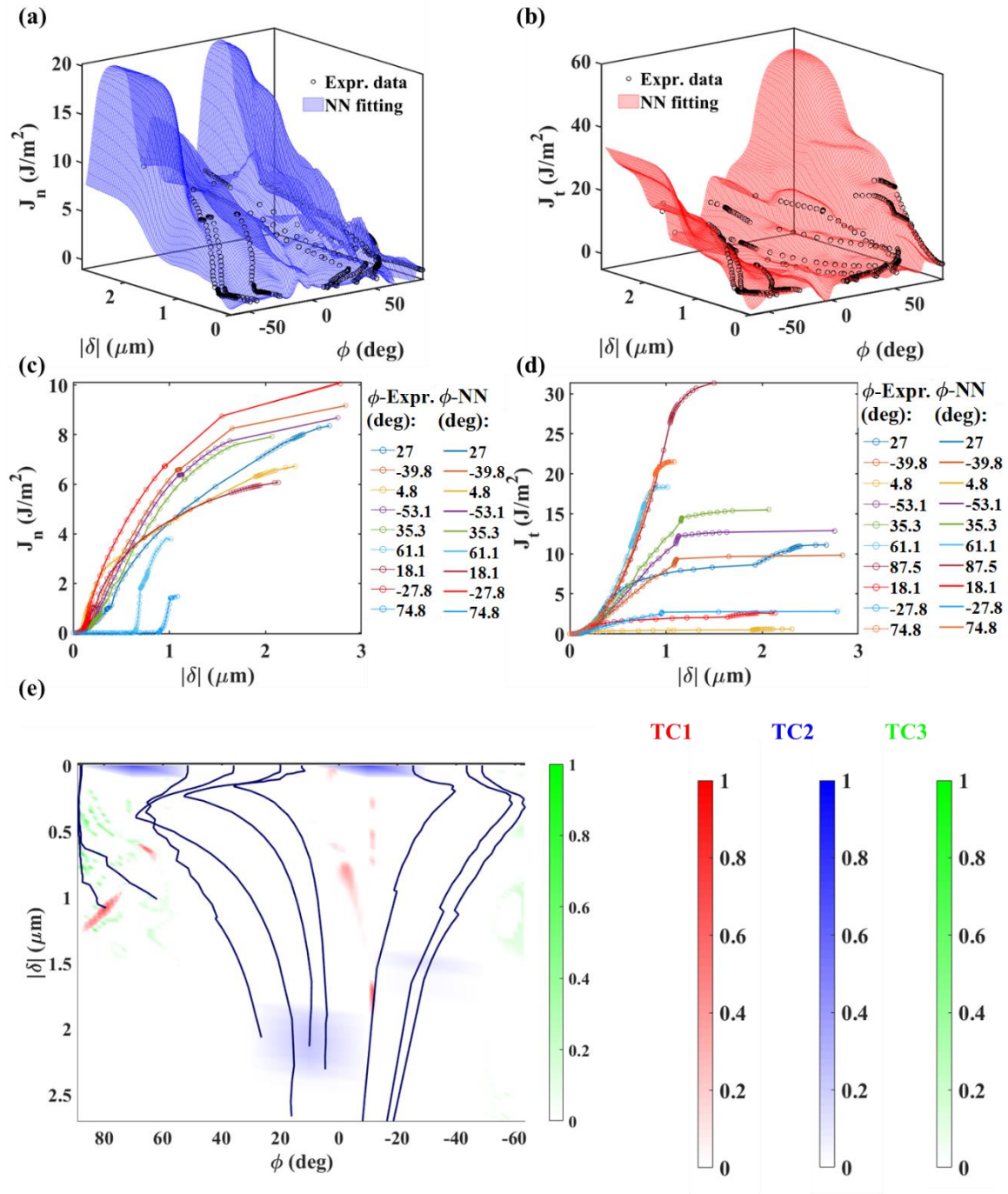


Fig. 16. (a-b) Modeled normal and tangential J-integral surfaces using TCNN with MSE and TC1, TC2, TC3 constraints (TCNN-set3) based on BO optimized weighting factors. (c-d) Modeling results for normal and tangential J-integrals comparing with experiment results. (e) Violation against each of the 3 TC conditions. The red contour shows violation against TC1 condition, blue contour for TC2 condition and green contour for TC3 condition. Black lines are experiment loading paths.



#### 4.4 Fitting error and TC condition violations

The modeling results with DNN, TCNN with different combinations of TC constraints (TCNN-set1 to TCNN-set3) and TCNN with BO optimized weighting factors are quantitatively evaluated from 2 perspectives: fitting with experiment results and violation rate to TC conditions. The results are shown in Fig. 17.

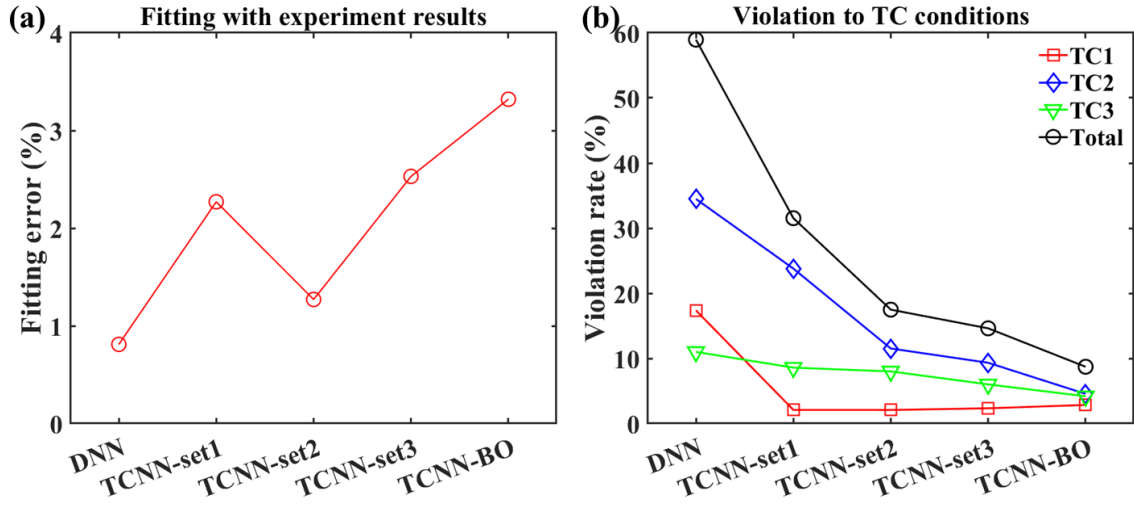


Fig. 17. (a) Fitting error comparing with experiment results used for training. (b) Violation rate to TC conditions.

The fitting error is defined as:

$$\text{Fitting error} = E \left( \|Y_i - Y_i^l\|_2^2 \right) \quad (24)$$

where  $Y_i$  and  $Y_i^l$  are  $i$ th point of true output and predicted output along experiment loading paths. As shown in Fig. 17a, the DNN result has the lowest error, and the TCNN with BO has the highest. All errors are below 4%, which is a low value that ensures the experimental information been learned by all data driven models.

The TC condition violation ratio is calculated with an area orientated definition and shown in Fig. 17b:

$$\text{Violation ratio} = \frac{A_V}{A_M} \quad (25)$$

where  $A_V$  is the area of the violation regions,  $A_M$  is the area of the overall modeling region. DNN modeling results have the highest violation ratio for all 3 TC conditions. The combined total ratio is larger than 0.5, which means that most part of the modeling results are against at least 1 TC conditions. This situation is significantly improved when modeling with TCNN, where different

TC constraints are applied as loss function terms. This improvement reached its limitation when 2 or 3 TC constraints are imposed, reflecting as the slightly increased violation ratio of TCNN-set3. This is due to the noise and system error induced confliction between experimental results and TC conditions. This confliction is mediated by BO optimization and a balance is reached between capturing the main trend of the experimental data and bypassing the local conflicting points. The total violation ratio is thus further improved.

## 5. Discussions and conclusions

In this paper, we proposed a TCNN approach that can provide a point-to-point modeling of interfacial traction-separation relations using only experimental data. The proposed model not only can provide robust predictions on mixed-mode traction-separation surfaces that capture the experimental data but also conform to physics laws, specifically the damage mechanics. This is achieved by fusing the neural network model with TC conditions requirements derived from rules of mechanics. In addition, with the integrated Bayesian optimization and weighing factors reflecting the priorities of the mechanical rules, the proposed TCNN approach can perfectly handle any conflicts between the experimental data and enforced TC conditions. This allows a “true” autonomous machine learning modeler that can provide rational constitutive models for material interfaces directly using experimental data. Numerical implementation results provide demonstrate the rigor of the proposed approach by comparison of modeling results with those from only neural network approaches.

Future studies will focus on rationalizing the prioritization of the weighing factors that applied to different TC conditions, as well as the application of TCNN to model traction-separation relations of other material interface that is interfered by other physics such as the diffusion field.

## References

1. Dugdale, D.S., *Yielding of steel sheets containing slits*. Journal of the Mechanics and Physics of Solids, 1960. **8**(2): p. 100-104.
2. Barenblatt, G.I., *The mathematical theory of equilibrium cracks in brittle fracture*. Advances in Applied Mechanics, 1962. **7**(1): p. 55-129.
3. Elices, M., et al., *The cohesive zone model: advantages, limitations and challenges*. Engineering fracture mechanics, 2002. **69**(2): p. 137-163.
4. Yang, Q. and B. Cox, *Cohesive models for damage evolution in laminated composites*. International Journal of Fracture, 2005. **133**(2): p. 107-137.



5. Turon, A., et al., *Accurate simulation of delamination growth under mixed-mode loading using cohesive elements: definition of interlaminar strengths and elastic stiffness*. *Composite structures*, 2010. **92**(8): p. 1857-1864.
6. Ungsuwarungsri, T. and W.G. Knauss, *The role of damage-softened material behavior in the fracture of composites and adhesives*. *International Journal of Fracture*, 1987. **35**(3): p. 221-241.
7. Park, K., H. Choi, and G.H. Paulino, *Assessment of cohesive traction-separation relationships in ABAQUS: A comparative study*. *Mechanics Research Communications*, 2016. **78**: p. 71-78.
8. Wittmann, F., et al., *Fracture energy and strain softening of concrete as determined by means of compact tension specimens*. *Materials and Structures*, 1988. **21**(1): p. 21-32.
9. Dong, J., et al., *Study on micro-scale properties of cohesive zone in shale*. *International Journal of Solids and Structures*, 2019. **163**: p. 178-193.
10. Camanho, P.P., C.G. Davila, and M. De Moura, *Numerical simulation of mixed-mode progressive delamination in composite materials*. *Journal of composite materials*, 2003. **37**(16): p. 1415-1438.
11. McGarry, J.P., et al., *Potential-based and non-potential-based cohesive zone formulations under mixed-mode separation and over-closure. Part I: Theoretical analysis*. *Journal of the Mechanics and Physics of Solids*, 2014. **63**: p. 336-362.
12. Park, K. and G.H. Paulino, *Cohesive zone models: a critical review of traction-separation relationships across fracture surfaces*. *Applied Mechanics Reviews*, 2013. **64**(6).
13. Needleman, A., *A continuum model for void nucleation by inclusion debonding*. 1987.
14. Freed, Y. and L. Banks-Sills, *A new cohesive zone model for mixed mode interface fracture in bimaterials*. *Engineering Fracture Mechanics*, 2008. **75**(15): p. 4583-4593.
15. Rose, J.H., J. Ferrante, and J.R. Smith, *Universal binding energy curves for metals and bimetallic interfaces*. *Physical Review Letters*, 1981. **47**(9): p. 675.
16. Needleman, A., *An analysis of tensile decohesion along an interface*. *Journal of the Mechanics and Physics of Solids*, 1990. **38**(3): p. 289-324.
17. Beltz, G. and J. Rice, *Dislocation nucleation versus cleavage decohesion at crack tips*. *Modeling the deformation of Crystalline Solids*, 1991: p. 457-480.

18. Kutz, J.N., *Deep learning in fluid dynamics*. Journal of Fluid Mechanics, 2017. **814**: p. 1-4.
19. Brunton, S.L., B.R. Noack, and P. Koumoutsakos, *Machine learning for fluid mechanics*. Annual Review of Fluid Mechanics, 2020. **52**: p. 477-508.
20. Wang, Z., et al., *Model identification of reduced order fluid dynamics systems using deep learning*. International Journal for Numerical Methods in Fluids, 2018. **86**(4): p. 255-268.
21. Huang, D., et al., *A machine learning based plasticity model using proper orthogonal decomposition*. Computer Methods in Applied Mechanics and Engineering, 2020. **365**: p. 113008.
22. Weber, G., M. Pinz, and S. Ghosh, *Machine Learning-Aided Parametrically Homogenized Crystal Plasticity Model (PHCPM) for Single Crystal Ni-Based Superalloys*. JOM, 2020: p. 1-16.
23. Eggersmann, R., et al., *Model-free data-driven inelasticity*. Computer Methods in Applied Mechanics and Engineering, 2019. **350**: p. 81-99.
24. Zhang, J. and M.D. Shields, *On the quantification and efficient propagation of imprecise probabilities resulting from small datasets*. Mechanical Systems and Signal Processing, 2018. **98**: p. 465-483.
25. Eriksson, D., et al. *Scalable global optimization via local bayesian optimization*. in *Advances in Neural Information Processing Systems*. 2019.
26. Zhao, M. and J. Li. *Tuning the hyper-parameters of CMA-ES with tree-structured Parzen estimators*. in *2018 Tenth International Conference on Advanced Computational Intelligence (ICACI)*. 2018. IEEE.
27. Ozaki, Y., et al. *Multiobjective tree-structured parzen estimator for computationally expensive optimization problems*. in *Proceedings of the 2020 Genetic and Evolutionary Computation Conference*. 2020.
28. Wu, C., R. Huang, and K.M. Liechti, *Simultaneous extraction of tensile and shear interactions at interfaces*. Journal of the Mechanics and Physics of Solids, 2019. **125**: p. 225-254.
29. Park, K., G.H. Paulino, and J.R. Roesler, *A unified potential-based cohesive model of mixed-mode fracture*. Journal of the Mechanics and Physics of Solids, 2009. **57**(6): p. 891-908.

30. Underwood, B.S., Y.R. Kim, and M.N. Guddati, *Improved calculation method of damage parameter in viscoelastic continuum damage model*. International Journal of Pavement Engineering, 2010. **11**(6): p. 459-476.
31. Rinaldi, A. and Y.-C. Lai, *Statistical damage theory of 2D lattices: Energetics and physical foundations of damage parameter*. International Journal of Plasticity, 2007. **23**(10-11): p. 1796-1825.
32. Swadener, J., K. Liechti, and Y. Liang, *Shear induced toughening in bonded joints: experiments and analysis*. International journal of fracture, 2002. **114**(2): p. 113-132.
33. Cordisco, F.A., et al., *Mode I fracture along adhesively bonded sinusoidal interfaces*. International Journal of Solids and Structures, 2016. **83**: p. 45-64.
34. Berggreen, C., B.C. Simonsen, and K.K. Borum, *Experimental and numerical study of interface crack propagation in foam-cored sandwich beams*. Journal of composite materials, 2007. **41**(4): p. 493-520.
35. Karpatne, A., et al., *Physics-guided neural networks (pgnn): An application in lake temperature modeling*. arXiv preprint arXiv:1710.11431, 2017.
36. Yang, Y. and P. Perdikaris, *Adversarial uncertainty quantification in physics-informed neural networks*. Journal of Computational Physics, 2019. **394**: p. 136-152.
37. Raissi, M., P. Perdikaris, and G.E. Karniadakis, *Physics-informed neural networks: A deep learning framework for solving forward and inverse problems involving nonlinear partial differential equations*. Journal of Computational Physics, 2019. **378**: p. 686-707.

## Supplementary Information

### S1. PPR model fitting with experimental TSR relations

To explore the possibility of fitting experimental data with existing analytical models, Monte Carlo simulations are used to fit experimental obtained TSR relations with PPR model. The normal and tangential tractions ( $\sigma_n, \sigma_t$ ) are derived by taking the gradient of the PPR potential and relate to the normal and tangential separations ( $\delta_n, \delta_t$ ) with,

$$\sigma_n = \frac{\Gamma_n}{\delta_n} \left( m \left( 1 - \frac{\delta_n}{\Delta_n} \right)^\alpha \left( \frac{m}{\alpha} + \frac{\delta_n}{\Delta_n} \right)^{m-1} - \alpha \left( 1 - \frac{\delta_n}{\Delta_n} \right)^{\alpha-1} \left( \frac{m}{\alpha} + \frac{\delta_n}{\Delta_n} \right)^m \right) \left( \Psi_t \left( 1 - \frac{\delta_t}{\Delta_t} \right)^\beta \left( \frac{n}{\beta} + \frac{\delta_t}{\Delta_t} \right)^n + \langle \psi_t - \psi_n \rangle \right) \quad (\text{S1a})$$

$$\sigma_t = \frac{\Gamma_t}{\delta_t} \left( n \left( 1 - \frac{|\delta_t|}{\Delta_t} \right)^\beta \left( \frac{n}{\beta} + \frac{|\delta_t|}{\Delta_t} \right)^{n-1} - \beta \left( 1 - \frac{|\delta_t|}{\Delta_t} \right)^{\beta-1} \left( \frac{n}{\beta} + \frac{|\delta_t|}{\Delta_t} \right)^n \right) \left( \Psi_n \left( 1 - \frac{\delta_n}{\Delta_n} \right)^\alpha \left( \frac{m}{\alpha} + \frac{\delta_n}{\Delta_n} \right)^m + \langle \psi_n - \psi_t \rangle \right) \frac{\delta_t}{|\delta_t|} \quad (\text{S1b})$$

where,  $\Delta_n, \Delta_t$  are characteristic length scale parameters where the  $\sigma_n, \sigma_t$  decrease to 0,  $\Psi_n, \Psi_t$  are energy constants,  $\psi_n, \psi_t$  are fracture energies where the subscripts  $n$  is for normal and  $t$  is for tangential.  $\alpha, \beta$  and  $m, n$  are shape parameters and non-dimensional exponents to be determined.

In these parameters,  $m, n$  are dependent on  $\alpha, \beta$  with:

$$m = \frac{\alpha(\alpha-1)\lambda_n^2}{(1-\alpha\lambda_n^2)} \quad (\text{S2a})$$

$$n = \frac{\beta(\beta-1)\lambda_t^2}{(1-\beta\lambda_t^2)} \quad (\text{S2b})$$

where,  $\lambda_n, \lambda_t$  is defined as  $\lambda_n = \Delta_{nc}/\Delta_n, \lambda_t = \Delta_{tc}/\Delta_t$  with  $\Delta_{nc}, \Delta_{tc}$  being the critical opening displacement where the  $\sigma_n, \sigma_t$  reach the peak value.  $\Psi_n, \Psi_t$  are dependent on  $\psi_n, \psi_t$  as well as  $m, n, \alpha, \beta$ :

$$\Psi_n = (-\psi_n) \frac{\langle \psi_n - \psi_t \rangle}{\psi_n - \psi_t} \left( \frac{\alpha}{m} \right)^m \quad (\text{S3a})$$

$$\Psi_t = (-\psi_t) \frac{\langle \psi_t - \psi_n \rangle}{\psi_t - \psi_n} \left( \frac{\beta}{n} \right)^n \quad (\text{S3b})$$

A total of 8 parameters are totally independent: length scales parameters,  $\Delta_{nc}, \Delta_{tc}$  and  $\Delta_n, \Delta_t$ ; energy parameters,  $\psi_n, \psi_t$ ; non-dimensional parameters,  $\alpha, \beta$ .

While fitting the experimental data with PPR models, we choose these parameters as variables to be optimized based on Eq. S1-S3. For each parameter, a varying range is specified based on the experimental data sets. For each modeling iteration, randomly generated values within each range is assigned to independent parameters, normal and tangential tractions corresponding to

separations along loading paths are calculated and compared to experimental data. A total of  $5.0 \times 10^6$  iterations are calculated and the parameter combination with least error is recorded. It is checked that value of each independent variables are within the range and not close to either upper or lower boundaries of pre-assumed range.

As shown in Fig. S2, along loading paths, both normal and tangential tractions have certain errors when comparing with experimental data, the main differences exist in the critical separations where tractions reach peak value or 0; the nonlinearity and Young's modulus of the elastic stage, the form of softening stages. These fitting results show that even being the most flexible analytical model, PPR models still lack complexity to capture the high level singularity real world experimental data shows, namely, the sharply increasing and decreasing around peak value traction points and varying characteristic separation values.

## S2. Fixed angle loading condition

For each monotonic loading case along fixed angle paths, the total J-integral ( $J_{total}$ ) is the summation of normal and tangential J-integral components, ie,

$$J_{total} = \int_{\Gamma} \sqrt{\sigma_n^2 + \sigma_t^2} d\delta = J_n + J_t = \int_{\Gamma} \sigma_n d\delta_n + \int_{\Gamma} \sigma_t d\delta_t \quad (S4)$$

where  $d\delta = \sqrt{1 + \tan^2 \phi} d\delta_n$ .

According to phase angle definition Eq. 1b, normal and tangential separations are related as,

$$\delta_t = \tan \phi \delta_n \quad (S5)$$

Plug Eq. S5 into Eq. S4,

$$\int_{\Gamma} \sigma_n d\delta_n + \int_{\Gamma} \sigma_t \tan \phi d\delta_n = \int_{\Gamma} \sqrt{(\sigma_n^2 + \sigma_t^2)(1 + \tan^2 \phi)} d\delta_n \quad (S6)$$

To make Eq. S6 holds for all  $d\delta_n$ , it requires that,

$$\sigma_n + \sigma_t \tan \phi = \sqrt{(\sigma_n^2 + \sigma_t^2)(1 + \tan^2 \phi)} \quad (S7)$$

Take square on both sides,

$$\sigma_n^2 + \sigma_t^2 \tan^2 \phi + 2\sigma_n \sigma_t \tan \phi = (\sigma_n^2 + \sigma_t^2)(1 + \tan^2 \phi) \quad (S8)$$

With proper transformation and Eq. S8 leads to,

$$\sigma_n^2 \tan^2 \phi + \sigma_t^2 - 2\sigma_n \sigma_t \tan \phi = 0 \quad (S9)$$

Thus,

$$(\sigma_n \tan \phi - \sigma_t)^2 = 0 \quad (S10)$$

Which leads to the fixed angle loading conditions,

$$\frac{\sigma_t}{\sigma_n} = \tan \phi = \frac{\delta_t}{\delta_n} \quad (S11)$$

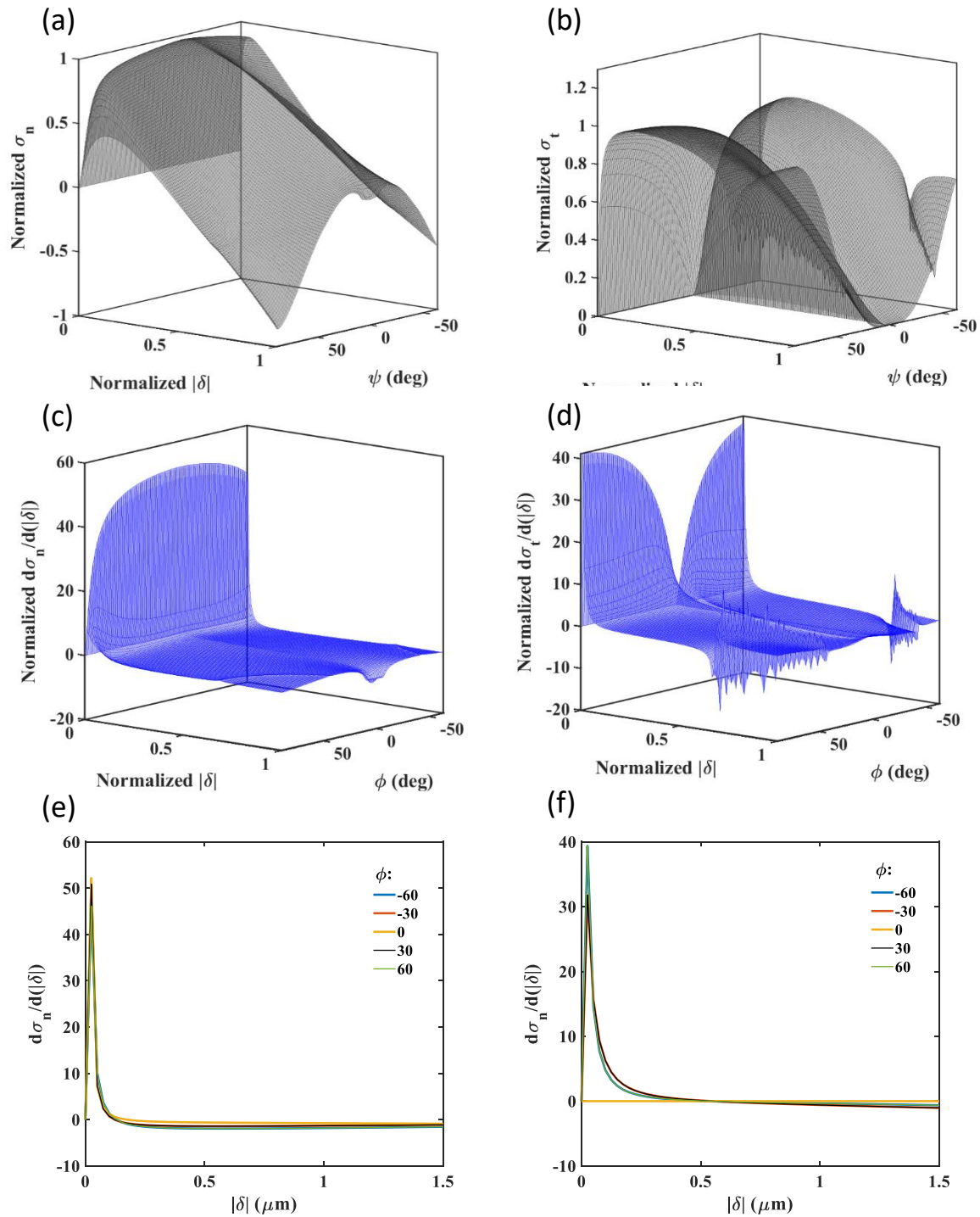


Fig. S1. (a-b), normalized PPR model for normal and shear stress versus phase angle ( $\phi$ ) and absolute separation ( $norm(\delta)$ ). (c-d) gradient surface of normal and shear stress. (e-f) gradient of normal and shear stress along fixed angle loading paths.

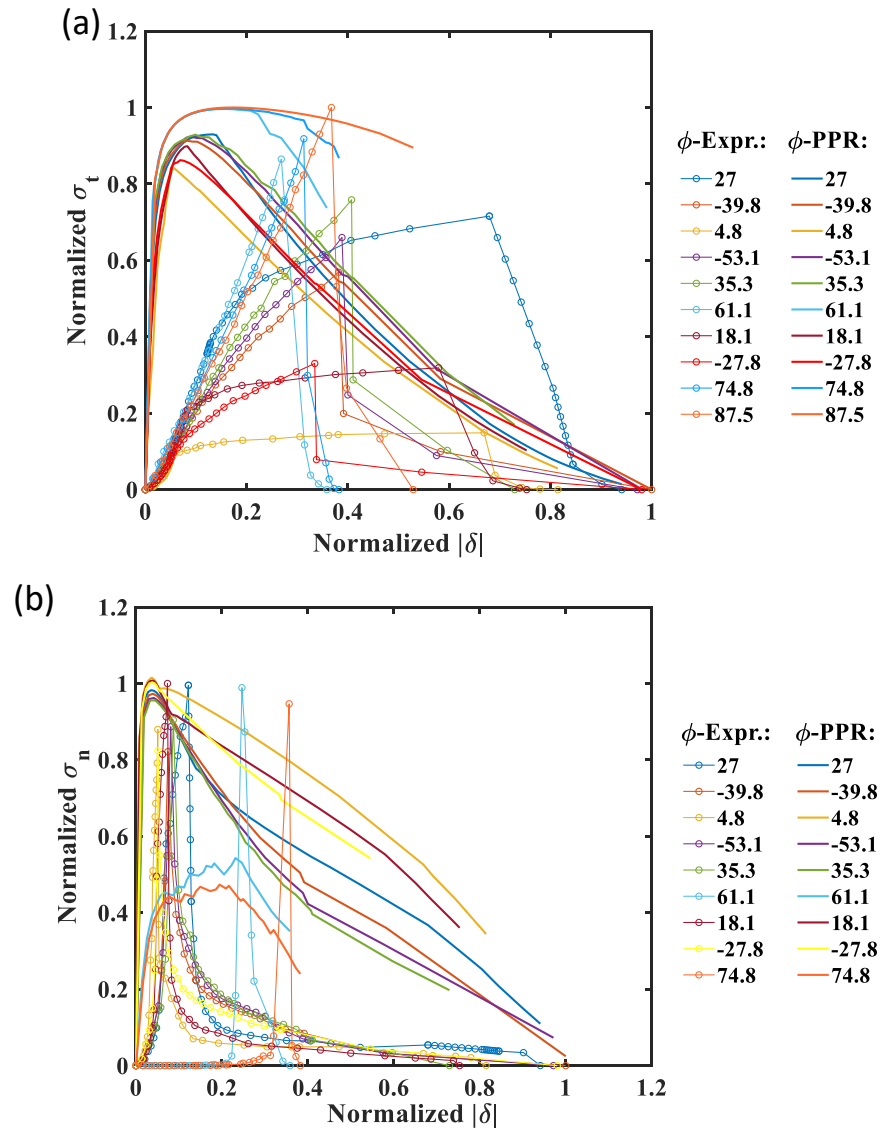


Fig. S2. (a-b), comparison for experimental and fitted tractions along experimental loading paths.